Reverse engineering the tropical precipitation-buoyancy relationship

Fiaz Ahmed and J. David Neelin

Atmospheric and Oceanic Sciences, University of California, Los Angeles, California

Submitted November 7th 2017

Revised January 21th 2018

Accepted February 23rd 2018

Journal of the Atmospheric Sciences

Corresponding author address:

Fiaz Ahmed

520 Portola Plaza

Math Sciences Building 7127

Los Angeles, CA 90095 email: fiaz@ucla.edu

Abstract

The tropical precipitation-moisture relationship, characterized by rapid increases in precipitation for modest increases in moisture, is conceptually recast in a framework relevant to plume buoyancy and conditional instability in the tropics. The working hypothesis in this framework links the rapid onset of precipitation to integrated buoyancy in the lower troposphere. An analytical expression that relates the buoyancy of an entraining plume to the vertical thermodynamic structure is derived. The natural variables in this framework are saturation and subsaturation equivalent potential temperatures, which capture the leading order temperature and moisture variations respectively. The use of layer averages simplifies the analytical and subsequent numerical treatment. Three distinct layers: the boundary layer, the lower-free troposphere and the mid-troposphere adequately capture the vertical variations in the thermodynamic structure. The influence of each environmental layer on the plume is assumed to occur via lateral entrainment, corresponding to an assumed mass flux profile. The fractional contribution of each layer to the mid-level plume buoyancy, i.e. the layer weight, is estimated from TRMM 3B42 precipitation and ERA-I thermodynamic profiles. The layer weights are used to "reverse-engineer" a deep inflow mass flux profile that is nominally descriptive of the tropical atmosphere through the onset of deep convection. The layer weights—which are nearly the same for each of the layers—constitute an environmental influence function and are also used to compute a free tropospheric integrated buoyancy measure. This measure is shown to be an effective predictor of onset in conditionally averaged precipitation across the global tropics—over both land and ocean.

1. Introduction

Conditional instability of the environment lies at the basis of moist convection, but quantifying the environmental influence on convection is a nontrivial exercise. An increase in tropospheric water vapor generally favors tropical convection (Sherwood 1999, Redelsperger et al. 2002, Chaboureau et al. 2004, Sherwood et al. 2004, Jensen and Del Genio 2006, Myoung and Nielson-Gammon 2010, Waite and Khouider 2010), but water vapor is only one among several influencing environmental factors. Moreover, the chaotic nature of convection renders its relationship to the environment non-unique. The use of statistics such as conditional means of convection-related quantities rather than individual convective events, however, can help elucidate the typical relationship to the environment. The statistics can in many ways be extremely revealing, as exemplified by the striking relationship between convection—represented by precipitation—and environmental moisture: rapid non-linear increases of precipitation with increases in atmospheric moisture content (Bretherton et al. 2004). A series of works (Peters and Neelin 2006, Peters et al. 2009, Neelin et al. 2009) have explored and documented the fine-scale (near instantaneous, $\leq 0.25°$ grids) precipitation-moisture relationship, along

with related statistics that arise when examining the probability distributions of precipitating and non-precipitating points, precipitation accumulation and cluster sizes. These statistics are collectively termed the convective transition statistics. The rapid increase in conditional precipitation is hereafter termed the precipitation onset. The onset is also observed in other related variables such as cloud top heights (Del Genio et al. 2012a). The observed precipitation onset can also be envisioned as the statistical representation of the precipitation increases associated with an ensemble of individual convective systems (Masunaga 2012), with organized convective systems contributing more to the rapid precipitation increases.

The proposed physical argument for the precipitation onset is buoyancy-centric. Holloway and Neelin, 2009 (hereafter HN09) showed using a steady-state entraining plume model that for environmental moisture values at and beyond precipitation onset, the entraining plumes are positively buoyant near the freezing level. The implication is that if a convective entity—often represented by a bulk-entraining plume—can survive mixing in environmental air and reach the freezing level, the subsequent buoyancy increases offered by the latent heat of fusion and smaller stratification in the upper troposphere will lead to strong precipitation. The tropical precipitation-moisture relationship is therefore primarily viewed as a precipitation-buoyancy relationship arising from the strong increase in convective rain. This buoyancy-centric view, however, does not directly account for frontal precipitation or stratiform rain (Houze 1997, Schumacher and Houze 2003), even though the latter is undoubtedly associated with the occurrence of buoyant convective rain.

Neelin et al. 2009 found, over the tropical oceans, that the bulk environmental moisture value associated with onset is sensitive to column-averaged tropospheric temperature ($\hat{T}$)—a warmer troposphere will show onset at a higher value of column water vapor (CWV). Empirical evidence therefore suggests that two bulk thermodynamic variables—CWV and $\hat{T}$—are sufficient to capture the variability in the shape of the precipitation onset curve across the tropical oceans. These bulk variables were primarily chosen as measures of convenience to capture the leading vertical thermodynamic structure. The efforts of this study will help interpret their behavior in a buoyancy-based framework, while taking higher order variations in the vertical structure into account.

The study of convective transition statistics has shown substantial utility in both mechanistic and diagnostic studies. For instance, recent works (Hannah et al. 2016, Allen and Mapes 2017) have suggested that the Lagrangian tracking of the CWV field can aid in interpreting salient synoptic variations in the tropics. Another avenue of research, directly relevant to this study is the question of entrainment, which can be found in the earliest treatises on the subject (Austin 1948, Houghton and Cramer 1951, Morton et al. 1956, Asai and Kasahara 1967). A satisfactory understanding and modeling of entrainment, has however, been problematic (see de Rooy et al. 2013 for a review) with well-documented consequences of ill-constrained entrainment on GCM simulations (see

Del Genio et al. 2012b for a review). Models are unduly sensitive to the value of entrainment that can compromise their ability to reproduce convective variability across time-scales ranging from sub-daily (Derbyshire et al. 2004; Jensen and Del Genio 2006; Wu and Del Genio 2010) to intraseasonal (Tokioka et al. 1988; Hannah and Maloney 2011) to even inter-annual (Neale et al. 2008). Agreement between convective transition statistics in models and observations is also sensitive to the assumed entrainment—a fact used to constrain its vertical profile and magnitudes in GCMs (Sahany et al. 2012, Kuo et al. 2017).

Observational studies of mesoscale convective systems (MCS, Houze 2004) provide another plausible pathway to constraining entrainment profiles, particularly with respect to deep, organized convection. Conceptual models and schematic depictions encapsulating decades of field observations describe thick or deep inflow layers (~ 5 km) feeding the convective portion of the MCS (Zipser 1977, Ferrier and Houze 1988, Pandya and Durran 1996, Kingsmill and Houze 1999a, Mechem et al. 2002 etc). These studies suggest that the idea of deep inflow of environmental air into the convective entity provides a conceptual springboard to begin describing environmental interactions with organized tropical convection. The deep inflow would naturally be relevant to the study of convective transition statistics, given that the precipitation onset is indeed a signature of organized convection (Masunaga 2012, Ahmed and Schumacher 2015).

This deep inflow approach was implemented in simple steady-state plume models (HN09, Schiro et al. 2016—hereafter SN16), replacing traditional mixing assumptions such as non-entraining or constant mixing plumes. These studies showed that the simple plume models are adept at qualitatively linking CWV values to the precipitation onset if the lateral entrainment is replaced with a prescribed environmental deep inflow: a constantly increasing mass-flux with height (from the surface to the mid-troposphere). This paradigm of entrainment is consistent with the updraft (or an ensemble of updrafts) interacting with an inflow of air that can include a coherent, *organized* component, instead of merely incorporating peripheral environmental air through small-scale turbulence. The convective transition statistics thus have potential to contribute constraints for reworking some of the basic assumptions about entrainment, as currently implemented in cumulus parameterization schemes.

The convective transition statistics over the tropical oceans have received much attention in the preceding decade, with only few recent investigations of these statistics over tropical land. Ahmed and Schumacher 2017, using satellite and reanalysis data, showed that land regions, during daytime, precipitation can attain onset at smaller column saturation fraction values than oceans, though they did not explore the $\hat{T}$ dependence. This tendency for precipitation onset in drier conditions over daytime land was also reported in Schiro (2017) who cautioned that vertical moisture variations over land could sometimes produce the same effect. Motivated by these apparent land-ocean differences, we will explore how they can be reconciled in a buoyancy-based framework, with our

efforts directed towards a consideration of the vertical thermodynamic structure.

The use of the bulk plume model—with the environmental influence determined by a deep layer of inflow—provides a physically intuitive path to relating convective transition statistics with its thermodynamic environment. This model will therefore be used to derive analytical expressions for plume buoyancy. We will employ θ_e (equivalent potential temperature)-based variables in constructing the expression for plume buoyancy. θ_e -based variables are more useful than moisture and temperature when expressing the approximate conservation properties of the bulk plume The environmental influence on the plume properties is expressed through an "influence function". Our expression for buoyancy creates a framework for empirically estimating this influence function. The application of this framework to the more reliable tropical oceanic observations (on account of uncertainties in surface emissivity over land, Prigent et al. 2006) yields an estimate of the influence function, whose validity is subsequently tested through application on tropical land data. Our results primarily emphasize the vertical parsing of the thermodynamic structure, but we find encouraging evidence that vertical averages from a few layers are sufficient to describe the convective transition statistics over both land and ocean.

The primary goal of this manuscript will be to introduce a buoyancy-based framework to interpret the known properties of the precipitation onset—including its CWV and $\hat{T}$ dependence—by incorporating information about the vertical thermodynamic structure. The data used for empirical analysis is described in Section 2. The influence function framework that relates precipitation onset to the environmental thermodynamic structure is introduced in Section 3. Within this physical hypothesis, instead of postulating an environmental influence function—in terms of weightings for each layer—and doing a forward calculation for buoyancy, section 4 asks the reverse question of what layer weights would be consistent with the observed precipitation onset. This empirical derivation of layer weights acts as a "reverse engineering" of the structure of the influence function. Section 5 presents the onset curves conditioned on a measure of buoyancy, contrasting it to convective transition statistics using bulk measures of CWV and ($\hat{T}$). A discussion of the results and concluding remarks are provided in Sections 6 and 7 respectively.

2. Data

Vertical profiles of temperature and specific humidity, surface variables including surface pressure, 2 meter temperature and dew point temperature were all obtained from the European Center for Medium Range Weather Forecast (ECMWF) Interim Reanalysis (ERA-Interim; Dee et al. 2011), 4 times daily at 0.25 degree grid spacing for a period spanning from September 2001 to December 2014. Concurrent values of precipitation were obtained from version 7 of the 3B42 Tropical Rainfall Measuring Mission (TRMM) Multi-Satellite Precipitation Analysis (TMPA) product (Huffman et al. 2007), also

available at a 0.25 degree resolution. The ERA-I data was processed and re-gridded to match the precipitation dataset.

The tropical oceanic regions were divided into four major basins: Indian Ocean [45E - 100E, 25S - 25N; 100E - 125E, 25S - 5S], Western Pacific Ocean [105 - 125E, 5S - 15N; 125E - 180E, 25N - 25S], Eastern Pacific Ocean [180 E - 100 W, 25S - 25N; 100W - 70W, 25S - 10N] and the Atlantic Ocean [70W - 15E, 25N - 25S]. The tropical land regions were divided into seven major regions: India [75E -90E, 5N - 25N], East Asia [105E - 125E, 15N - 25N], Maritime Continent [95E - 145E, 10S - 10N], Australia [125E - 145E, 20S - 10S], South America [75W - 50W, 10S - 10N], Argentina [75W - 50 W, 25S - 15S] and West Africa [17W - 10 E, 0 - 15N]. The land regions typify different regimes of tropical continental convection (Xu and Zipser 2012), but are not seasonally distinguished in this study. Note that a land-sea mask was applied to ensure that selected grid points in the specified intervals did not contain data from both land and ocean.

The remote sensing based estimates of both precipitation and CWV—which rely on passive microwave imagers—suffer from greater uncertainty over land than over oceans, owing to uncertainties in the estimates of the background surface emissivity (Prigent et al. 2006, Tian et al. 2014). The satellite radiances are not assimilated into the ERA-I dataset over land and the moisture field is therefore less constrained by observations; the possibility that some of the land-ocean differences in the convective transition statistics reported in this study originate from this instrument uncertainty over land is a noteworthy caveat. We performed a comparison between CWV values from ERA-I and those from tropical Atmospheric Radiation Measurement (ARM) ground sites. These sites included one land site in Manacapuru, Brazil (part of the Green Ocean Amazon (GoAmazon2014/5) field campaign; Martin et al. 2016) and two oceanic sites in the tropical Western Pacific: Nauru and Manaus. We found that over these three sites, the ERA-I moisture values and the resulting precipitation curves validated fairly well (see Supplement: Figures S1, S2 and S3).

3. The environmental influence function

Both HN09 and SN16 used a steady-state deep-inflow plume model to show that there is a strong correlation between freezing-level buoyancy and the CWV value around which the *in situ* precipitation shows onset. The results from both these studies suggest that a plume rising out of the boundary layer that can survive dilution and reach the freezing level will develop to be *strongly buoyant* in the upper troposphere. This is due to contributions from the latent heat of fusion, as well as smaller values of static stability in the upper troposphere. Both these studies also demonstrated the utility of diagnosing the amount of environmental air entering the plume (the inflow) at each level from vertical gradients in an assumed mass-flux profile.

The actual nature of entrainment into the plume requires some elaboration. Entrainment is often partitioned into dynamic and turbulent forms, with the former

denoting the flux of environmental air into the cloud that must satisfy mass-continuity in the presence of vertical motions, while the latter is attributed to small-scale turbulence on the cloud-edge (e.g. Houghton and Cramer 1951, Asai and Kasahar 1967, Masunaga and Luo 2016 etc.) This partition, in some sense is artificial, since both turbulent and dynamic forms of entrainment can cause an increase in mass-flux with height and therefore collectively satisfy mass continuity. Morisson 2017, for instance, found that the dynamic and turbulent modes of entrainment are tightly linked. In our framework, we are looking to quantify the influence of the environmental air on plume properties, such as buoyancy. We are not interested in the modes of the environmental air transfer—dynamic or turbulent—*per se*. We now introduce the different measures of buoyancy that will feature in this study.

3.1 Quantifying environmental influence on convection

Consider a steady-state bulk plume with a property that is conserved in the updraft, ϕ_u. Assume that the corresponding environmental value $\tilde{\varphi}_e$ interacts with the plume through an influence function $I(z,z')$, such that $\varphi_u(z)$ at any vertical level z can be written as:

$$\phi_u(z) = \int_0^z I(z,z')\tilde{\phi}_e(z')dz' \tag{1}$$

In this formulation $\tilde{\varphi}_e$ at any level z' can affect the plume property at level z; $I(z,z')$ can therefore be thought of as a Green's function (Larson 1997). $I(z,z')$ incorporates modes of environmental influence on the plume: turbulent and dynamic entrainment and detrainment. To simplify the physical interpretation, we now outline the connection to mass flux and the traditional entrainment parameter. Under certain simplifying assumptions:

$$I(z,z') = \frac{1}{M(z)}\frac{\partial M(z')}{\partial z'} \tag{2}$$

where $M(z)$ is the vertical mass flux at level z. $I(z,z')$, as defined in (2) would correspond to what is traditionally termed dynamic entrainment. In this definition, dynamic entrainment is the only pathway through which the environment influences the plume, though other forms of interaction (turbulent entrainment, detrainment etc.) can be incorporated at the expense of analytical simplicity. For the case (2), (1) can be written as:

$$\phi_u(z) = \frac{1}{M(z)}\int_0^z \frac{\partial M}{\partial z'}\tilde{\phi}_e(z')dz' \tag{3}$$

Note that the differential form of (3) is:

$$\frac{\partial(M\phi_u)}{\partial z} = \frac{\partial M}{\partial z}\tilde{\phi}_e \tag{4}$$

As we are not considering detrainment and turbulent entrainment, we can re-write (4) as:

$$\frac{\partial\phi_u(z)}{\partial z} = -\varepsilon(\phi_u(z) - \tilde{\phi}_e(z)) \tag{5}$$

where $\varepsilon = \frac{1}{M(z)}\frac{\partial M(z)}{\partial z}$ is the entrainment. (5) is the standard entraining plume equation (Betts 1975, Jakob and Siebesma 2003, Siebesma et al. 2007) ,which is the starting point for several works that study the influence of lateral mixing on plume properties. (5) is also valid when both detrainment and entrainment are accounted for (e.g. see the derivation in Masunaga and Luo, 2016). It is worth noting potential advantages of using the integral form (3) over the differential form (5). In (5), the plume property at level z is dependent only on the local mixing coefficient, ε — implying that all of the mixing is local and complete. On the contrary, the use of $I(z,z')$ in (3) makes it clear that the entrained environmental air at level z does not have to undergo local mixing, but can mix anywhere in the levels between z and z'. Moreover (5) implies that φ_u should be differentiable at all points in the vertical, making the estimation of entrainment problematic if the vertical mass flux profile is noisy. The expression in (3), on the other hand, allows one to smooth over noisy profiles of $\frac{\partial M}{\partial z}$ to produce more robust values for $\varphi_u(z)$.

Note that the non-local view of mixing as captured by $I(z,z')$ is also embodied in the *transilient matrix* (Stull 1993, Larson 1997, Romps and Kuang 2011) that seeks to represent the fractional mass contribution of every level in a column to every other level in matrix form.

3.2 Candidate buoyancy measures

We start with the hypothesis that an appropriate measure of plume buoyancy can help relate conditionally averaged precipitation to the environmental thermodynamic properties. More specifically, we are interested in buoyancy measures that can potentially help capture the precipitation onset—or the sharp increase in precipitation with increase in buoyancy. For this purpose, we propose two conceptually useful candidate buoyancy measures:

1. B_{int}, the integrated buoyancy from the top of the boundary layer to the freezing level. This measure is similar to an entraining Convective Available Potential

Energy that is used in the closure part of convective parameterization schemes (Zhang and McFarlane 1995) and is useful in capturing the bulk properties of the lower troposphere.

2. B_F, the buoyancy at the freezing level. This measure was chosen based on the results from HN09 and SN16, who showed that B_F increased with CWV under appropriate mixing assumptions—potentially acting as the threshold for convective onset. B_F explicitly clarifies that the plume is buoyant at the freezing level (distinguishing from circumstances where there might be high buoyancy at lower levels but no buoyancy at the level required for the transition to deep convection)

We use these two buoyancy measures in a complementary manner. B_F yields simple expressions that aid physical insight and parameter estimation. It also provides clarity on buoyancy at a vertical level appropriate to deep convection. It is used to derive parameters that are then tested using B_{int}. Specifically, we will test whether the conditional precipitation can be captured by a relationship of the form:

$$< P >= f(B) \tag{6}$$

Where B is a candidate buoyancy measure. We anticipate that the relationship (6) will yield the canonical precipitation-moisture curve, when moisture acts as a proxy for the plume buoyancy.

3.3 Analytical expressions for buoyancy

We now seek to represent B_{int} and B_F in terms of the vertical thermodynamic structure. Both these measures are constrained by the freezing level that has both a physical justification (from the results of HN09 and SN16) and the advantage of making the analytical treatment easier by neglecting the ice-phase physics. The emphasis on the buoyancy below the freezing level does not exclude potential relations to buoyancy above, but is hypothesized to give the leading behavior, since the convective plume has to reach the freezing level for deep convection to be initiated.

We assume that the bulk plume undergoes reversible moist-adiabatic liquid-vapor transformations and therefore conserves its equivalent potential temperature θ_e. This assumption breaks down in the upper levels of the heavily precipitating environments due to the irreversible loss of moisture. We are, however, primarily interested in the lower tropospheric buoyancy, below the freezing level, where the assumption of reversible moist adiabatic transformations is more permissible. We split the environmental equivalent potential temperature $\tilde{\theta}_e$ into its saturated and sub-saturated components, representing the temperature and moisture components respectively.

$$\tilde{\theta}_e = \underbrace{\tilde{\theta}_e^{\,*}}_{\textit{saturated}\ \text{eq. pot. temp.}} - \underbrace{\tilde{\theta}_e^{\,+}}_{\textit{subsaturation}} \tag{7}$$

The subsaturation θ_e^+, measured by the difference between θ_e and θ_e^*, is the additional moist entropy that will bring an environment to saturation. Similar subsaturation measures have featured in past theoretical works (e.g. the "saturation deficit" in Raymond (2000) and "anomalous moisture deficit" in Kuang (2008)). θ_e^+ has both temperature and moisture dependence, but in practice, much of its variations are controlled by moisture variations. Example θ_e^+ profiles for two contrasting environments—one dry and the other moist are shown in Figure 1a.

We also define the plume buoyancy B as:

$$B(z) = g\left(\frac{\theta_e(z) - \tilde{\theta}_e^{\,*}(z)}{\tilde{\theta}_e^{\,*}(z)}\right) \tag{8}$$

The traditional formulation of buoyancy is $g\left(\frac{T_{vp} - \overline{T}_v}{T_{vp}}\right)$, where T_{vp} and $\overline{T}_v$ are the plume and environment virtual temperatures respectively, so our formulation differs from the traditional formulation in its omission of the virtual temperature effects.

Using (3) and (8) for $\varphi_u = \theta_e$ and assuming zero mass flux (or influence) at the surface, we get an expression for the buoyancy B in height coordinates:

$$B(z) = g\frac{1}{M(z)\tilde{\theta}_e^{\,*}(z)}\left(-\int_0^z \frac{\partial M}{\partial z'}\tilde{\theta}_e^{\,+}(z')dz' + \int_0^z \frac{\partial M}{\partial z'}\tilde{\theta}_e^{\,*}(z')dz'\right) - g \tag{9}$$

and a similar expression in pressure coordinates:

$$B(p) = g\frac{1}{M(p)\tilde{\theta}_e^{\,*}(p)}\left(-\int_{p_s}^{p} \frac{\partial M}{\partial p'}\tilde{\theta}_e^{\,+}(p')dp' + \int_{p_s}^{p} \frac{\partial M}{\partial p'}\tilde{\theta}_e^{\,*}(p')dp'\right) - g \tag{10}$$

Where p_s is the surface pressure. (10) can be expressed as:

$$B(p) = \frac{g}{\overline{\theta}_e^{\,*}(p)}\left(-\int_{p_s}^{p} I(p,p')\tilde{\theta}_e^{\,+}(p')dp' + \int_{p_s}^{p} I(p,p')\tilde{\theta}_e^{\,*}(p')dp'\right) - g \tag{11}$$

Where the $I(p,p')$ is the influence function, defined here as $I(p,p') = \frac{1}{M(p)}\frac{\partial M(p')}{\partial p'}$.

The plume buoyancy at any level p is therefore given by vertical profile of the environmental θ_e^* and θ_e^+ weighted by the influence function at all levels below p. As stated above, the influence function is related to the vertical mass-flux profile in presence of dynamic entrainment alone. So within this framework, knowledge of the influence function is tantamount to the knowledge of the mass-flux profile and vice-versa.

Any assumed mass-flux profile can be used to yield an expression for plume buoyancy from (11). We assume the existence of a piecewise, monotonically increasing mass-flux profile as depicted in Figure 1 and note that this deep inflow profile is similar in form to the mass-flux and vertical velocity profiles derived from tropical observations (LeMone and Zipser 1980, Mapes and Houze 1995, Kumar et al. 2015, Schumacher et al. 2015; Masunaga and Luo 2016 etc.). We assume three distinct layers in the vertical to capture the variations in the rate of inflow with a few degrees of freedom. The vertical averages in each of these layers naturally emerge as the relevant variables in the analytical framework, associated with the piecewise linear assumption on the mass flux. Note that the rates of increase of mass flux in each layer are not assumed in advance — rather these are to be determined in the subsequent empirical analysis.

The choice of layers in the empirical analysis should reflect physically reasonable considerations, both for the form of a mass flux and for the environmental variables that will thus be weighted. The number of vertical degrees of freedom must also be modest enough to be tractable for analysis with available data. The boundary layer is one natural distinct layer to consider. The free troposphere is further delineated into two portions, which will be hereby termed the lower and the middle free tropospheric layers. This distinction was imposed after it appeared that there exists a degree of coherence in vertical structure of moisture within these layers (see Supplement, Figure S4). Coherent variations in these layers are also seen in the tropical sounding data (e.g. see Figure 2a in HN09).

Thus, our assumed deep inflow mass flux profile (Figure 1b) has the piecewise-linear form:

$$M(p)=\begin{cases} a(p_s-p), & \mathrm{p_B} \le \mathrm{p} < \mathrm{p}_s \\ a(p_s-p_B)+b(p_B-p), & \mathrm{p}_L \le \mathrm{p} < \mathrm{p}_B \\ a(p_s-p_B)+b(p_B-p_L)+c(p_L-p), & \mathrm{p}_L \le \mathrm{p} < \mathrm{p}_L \end{cases} \tag{12}$$

The layer interface heights p_B, p_L and p_F represent the heights of the boundary layer, lower-free troposphere and the freezing level respectively. a, b and c here are the magnitudes of the mass flux gradients, representing the inflow intensity in each layer..

The plume buoyancy at level p can now be written in terms of layer averages:

$$B(p)=g\left(\frac{a\Delta p_B}{M(p)\tilde{\theta}_e^{\,*}(p)}\left\langle\tilde{\theta}_e\right\rangle_{BL}-\frac{b}{M(p)\tilde{\theta}_e^{\,*}(p)}\int_p^{p_B}\tilde{\theta}_e^{\,+}(p')dp'+\frac{b}{M(p)\tilde{\theta}_e^{\,*}(p)}\int_p^{p_B}\tilde{\theta}_e^{\,*}(p')dp'-1\right)$$

for $p_L \le p < p_B$

and

$$B(p) = g\left(\frac{a\Delta p_B}{M(p)\tilde{\theta}_e^{\,*}(p)}\left\langle \tilde{\theta}_e \right\rangle_{BL} - \frac{b\Delta p_L}{M(p)\tilde{\theta}_e^{\,*}(p)}\left\langle \tilde{\theta}_e^{\,+} \right\rangle_{L} + \frac{b\Delta p_L}{M(p)\tilde{\theta}_e^{\,*}(p)}\left\langle \tilde{\theta}_e^{\,*} \right\rangle_{L} \right.$$
$$\left. - \frac{c}{M(p)\tilde{\theta}_e^{\,*}(p)}\int_p^{p_L} \tilde{\theta}_e^{\,+}(p')dp' + \frac{c}{M(p)\tilde{\theta}_e^{\,*}(p)}\int_p^{p_L} \tilde{\theta}_e^{\,*}(p')dp' - 1 \right) \qquad (13)$$

$$\text{for } p_M \le p < p_L$$

Where the angular brackets denote vertical averages and Δ denotes the pressure thickness in each layer. One of our candidate buoyancy measures B_{int} is the integrated buoyancy from the top of the boundary layer to the freezing level, normalized by the pressure thickness to retain units of buoyancy:

$$B_{\text{int}} = \frac{\int_{p_L}^{p_B} B(p)dp + \int_{p_M}^{p_L} B(p)dp}{(p_B - p_M)} \qquad (14)$$

Two further simplifications are made to estimate B_{int}:

1. $\frac{1}{\tilde{\theta}_e^{\,*}(p)}$ is replaced with its layer average $\frac{1}{\left\langle \tilde{\theta}_e^{\,*} \right\rangle}$, assuming that deviations from the layer average $\tilde{\theta}_e^{\,*}$ are small within each layer.
2. $\int_p^{p_\#} \tilde{\theta}_e^{\,\#}(p')dp'$ is replaced with $\left\langle \tilde{\theta}_e^{\,\#} \right\rangle_{LA}\left(p_\# - p\right)$, where $\theta_e^{\,\#}$ represents $\theta_e^{\,*} or\ \theta_e^{\,+}$ and $p_\#$ is the layer interface height representing p_L or p_M and $\left\langle \overline{\theta}_e^{\,\#} \right\rangle_{LA}$ is the layer average. This is equivalent to assuming that the subsaturation and saturation variables are invariant within the layers being considered. This invariance assumption approximates strong linear correlations of $\theta_e^{\,*} or\ \theta_e^{\,+}$ within the layer.

B_{int} can then be written as a linear combination of layer-averaged variables:

$$B_{\text{int}} = \frac{g}{(p_B - p_M)}\left\{ A\frac{\left\langle \tilde{\theta}_{eBL} \right\rangle}{\left\langle \tilde{\theta}_{eL}^{\,*} \right\rangle} + B\left(1 - \frac{\left\langle \tilde{\theta}_{eL}^{\,+} \right\rangle}{\left\langle \tilde{\theta}_{eL}^{\,*} \right\rangle} \right) + C\frac{\left\langle \tilde{\theta}_{eBL} \right\rangle}{\left\langle \tilde{\theta}_{eM}^{\,*} \right\rangle} + D\left(\frac{\left\langle \tilde{\theta}_{eL}^{\,*} \right\rangle}{\left\langle \tilde{\theta}_{eM}^{\,*} \right\rangle} - \frac{\left\langle \tilde{\theta}_{eL}^{\,+} \right\rangle}{\left\langle \tilde{\theta}_{eM}^{\,*} \right\rangle} \right) + E\left(1 - \frac{\left\langle \tilde{\theta}_{eM}^{\,+} \right\rangle}{\left\langle \tilde{\theta}_{eM}^{\,*} \right\rangle} \right) - 1 \right\}$$

(15)

(15) yields B_{int} as a linear combination of five different terms—involving the boundary layer equivalent potential temperature $\left\langle \tilde{\theta}_{eBL} \right\rangle$, the mid and lower tropospheric subsaturation terms ($\left\langle \tilde{\theta}_{eL}^{\,+} \right\rangle, \left\langle \tilde{\theta}_{eM}^{\,+} \right\rangle$) and saturation terms ($\left\langle \tilde{\theta}_{eL}^{\,*} \right\rangle, \left\langle \tilde{\theta}_{eM}^{\,*} \right\rangle$). Note that increases in atmospheric moisture are not enough to guarantee increases in B_{int}, which is also determined by the magnitudes of the free tropospheric temperature as well as the

boundary layer moist entropy. The coefficients A-E in (15) are functions of the *relative* inflow intensities and the pressure thicknesses in each layer (see Supplement). The relative inflow intensities take the form of ratios such as $\frac{a\Delta p_B}{a\Delta p_B + b\Delta p_L}$ and $\frac{a\Delta p_B + b\Delta p_L}{a\Delta p_B + b\Delta p_L + c\Delta p_M}$ etc., whose estimation allows us to diagnose the vertical influence function $I(p,p')$. The next section describes how we can empirically estimate these layer weightings by evaluating the precipitation onset as a function of the different layer averages of $\tilde{\theta}_e^{+}$ and θ_{ed}^{*}, which are the linear components of the integral in (11).

4. **Empirical estimation of the layer weights**

4.1 Use of freezing level buoyancy

While (15) allows us to compute B_{int}, given an estimate of the different layer weightings, it is in a form that is not tractable for the estimating those layer coefficients themselves. So consider the alternative buoyancy measure proposed in Section 3.2: B_F , freezing-level buoyancy, which is given by the following expression:

$$B_F = g\frac{1}{M(p)\tilde{\theta}_e^{*}(p)}\left(a\Delta p_B\left\langle\tilde{\theta}_{eBL}\right\rangle - b\Delta p_L\left\langle\tilde{\theta}_{eL}^{+}\right\rangle - c\Delta p_M\left\langle\tilde{\theta}_{eM}^{+}\right\rangle + d\left\langle\tilde{\theta}_e^{*}\right\rangle_{Deep}\right) - g \qquad (16)$$

This expression is obtained directly from (13), (by substituting $p=p_M$, the freezing level pressure). This expression assumes a degree of vertical coherence in the saturation equivalent potential temperature structure between the lower free troposphere and mid-troposphere (as shown in Holloway and Neelin 2007) and their linear combination is condensed to one variable $\left\langle\tilde{\theta}_e^{*}\right\rangle_{Deep}$, which is assuming a single vertical mode of temperature variation in the free troposphere that tracks some of the variations in $\hat{T}$. Note that in this expression, $d = b\Delta p_L + c\Delta p_M$.

We observe that (16) is a linear combination of the inflow intensities and the pressure thicknesses in each layer. This form is simpler than the expression for the integrated buoyancy in (15), in that it directly involves the use of the layer-averaged inflow coefficients. As mentioned in Section 3, we expect that the freezing-level buoyancy B_F should also be an effective discriminant in predicting the precipitation onset as it determines the fate of the plumes transitioning to deep convection (i.e. identifies plumes with adequate buoyancy to extend into the upper troposphere). There are exceptions to this statement, when considering the influence of the free tropospheric temperature variations, which we will elaborate on towards the end of this section. For the estimation of layer weights, we will use the conjecture that $< P >= f(B_F)$.

4.2 Precipitation onset in θ_e-based variables

We first proceed by testing if the precipitation shows the same rapid increase when binned by the layer-averaged buoyancy-centric variables in θ_e-based variables, as it does with the bulk variables CWV and $\hat{T}$. We first re-write the freezing level buoyancy from (16) in the form:

$$B_F = g\left(\frac{a\Delta p_B}{M(p_F)}\theta_{eBL} - \frac{b\Delta p_L}{M(p_F)}\theta_{eL}^{+} - \frac{c\Delta p_M}{M(p_F)}\theta_{eM}^{+} + \frac{d}{M(p_F)}\theta_{ed}^{*} - 1 \right) \qquad (17)$$

Where we have written the environmental layer averages without the tilde and angular brackets. These layer averages are also normalized by the equivalent saturation potential temperature at the freezing level, which eliminates the $\theta_e^*(p)$ term from the denominator in (16).

We bin the precipitation over each of the tropical oceans in terms of the four θ_e-based variables in (16). In computing the layer averages, we adopt sigma coordinate-like definitions to keep track of the variable surface pressure values—especially between land and oceans. The boundary layer is defined as a 100 mb thick layer from the surface. The lower troposphere, as a 150 mb thick layer from the top of the defined boundary layer and the mid-troposphere as the layer that is bounded by the top of the lower-free troposphere and the 500 mb pressure level. These definitions are necessary because of the sensitivity of the precipitation onset over land to the variations in surface pressure—substantially arising from orography. See Supplement (Figure S4) for more information. In this case, the layer average of the saturation equivalent potential temperature between 500 - 600 mb is used to normalize the variables and the resulting quantities are multiplied by a reference value (340 K).

The precipitation over the tropical oceanic basins is first binned by three of the four variables that were obtained from the right-hand side of the expression in (16) (θ_{eBL}, θ_{eL}^{+} and θ_{ed}^{*}). To ensure adequate sampling in each ocean basin, variations of θ_{eM}^{+} are not included in this binning procedure.

Figure 2 shows the precipitation as a function of θ_{eL}^{+} (the lower-tropospheric subsaturation), for roughly constant values of θ_{ed}^{*} and θ_{eBL}. The x-axis is reversed for subsaturation here and in subsequent figures so that moisture increases to the right as subsaturation decreases. Precipitation shows a strong increase with decrease in θ_{eLT}^{+}, resembling the well-known precipitation-moisture curves. This result is encouraging, since the precipitation onset with increasing column moisture is captured with variables that directly relate a buoyancy measure to the environmental thermodynamic structure. There is also good agreement between the precipitation onset curves for the different tropical ocean basins, barring slight variation in the slope of the curves (e.g. in Figures 2c, e, f, i and j).

4.3 Collapse procedures

The near-uniform behavior of the precipitation onset as a function of θ_e-based variables over the different tropical ocean basins in Figure 2 suggests that all the ocean points can be grouped together. This unified tropical ocean sample set now yields enough points to bin precipitation by four variables, now including θ_{eM}^{+}. Following the four-dimensional binning, we proceed to empirically estimate values for the coefficients ($\frac{a\Delta p_B}{M(p_F)}$, $\frac{b\Delta p_L}{M(p_F)}$ and $\frac{c\Delta p_M}{M(p_F)}$) in (17) and begin by describing the procedure employed.

To motivate the procedure, we start with the physical hypotheses that there exists a *threshold freezing-level buoyancy* for precipitation onset given by B_T, such that increases in B_F above B_T lead to strong increases in conditionally averaged precipitation. In other words, we assume that $< P >= f(B_F)$ and that f captures the strong non-linearity associated with precipitation onset. The expectation from the expression for B_F in (17) is that the various factors from different layers affecting can compensate for each other in reaching allowing B_F to reach the threshold for precipitation onset, B_T. Consider a thermodynamic profile with $B_F = B_T$, where B_F can be modified by changing any of its four components in (17). For example, assume that two of these four components, say θ_{eBL} and θ_{ed}^{*} are held constant and only θ_{eM}^{+} and θ_{eL}^{+} are allowed to vary. Now an imposed change in the θ_{eM}^{+} component, $\delta\theta_{eM}^{+}$ will change B_F. The conditional precipitation will still increase rapidly at $B_F = B_T$, provided that there is a compensating change in θ_{eL}^{+}, $\delta\theta_{eL}^{+}$. If we can measure the ratio of the changes in the two components $\frac{\delta\theta_{eL}^{+}}{\delta\theta_{eM}^{+}}$ required to produce the same precipitation-buoyancy curve, then we can obtain a measure of $-\frac{c\Delta p_M}{b\Delta p_L}$.

We now translate this into a more general procedure using the conditional-average precipitation <P> dependence on the θ_e –based variables. Specifically, we are asking what shifts in one of the variables are required to compensate for changes in one of the others to collapse the <P> dependence as closely as possible to a single function. During this procedure we can also note any departures from this, and can subsequently test how well this procedure works overall.

Figure 3a shows the precipitation as function of θ_{eM}^{+} and θ_{eL}^{+}, holding θ_{eBL} and θ_{ed}^{*} constant (to within binning accuracy). Note that the bin resolution is coarse for θ_{eMT}^{+}, θ_{ed}^{*} and θ_{eBL} (2 K) and finer for θ_{eL}^{+} (0.5 K); the coarse bin sizes are necessary to ensure that enough samples are present in each bin to yield precipitation onset. *This binning procedure is the data analysis version of holding two variables constant, while*

allowing the other two to vary, as described in the previous paragraph. Onset curves corresponding to different values of θ_{eM}^{+} are marked by different colors. Note that these precipitation curves are variants of the canonical precipitation-moisture curves, with subsaturation variations acting as the surrogates for the usual moisture variation. Also note that weak precipitation can occur for a near–saturated mid-troposphere (θ_{eMT}^{+}=1 K in orange and θ_{eMT}^{+}=3 K in red), even when the lower-troposphere is far from saturation. This weak precipitation contribution is likely corresponds to the regime of large-scale precipitation that occurs when the midtroposphere saturates, but the lower free troposphere is too far from saturation to permit conditional instability. The rapid increase in precipitation as θ_{eL}^{+} is decreased corresponds to the onset of deep convection, which is the object of interest here. This precipitation onset happens at higher values of θ_{eL}^{+} for lower values of θ_{eM}^{+}. *This behavior is physically interpreted as increases in B_F (that arise from a moister mid-troposphere) leading to precipitation onset in a drier lower free troposphere,* i.e. that we have compensation between the contributions of θ_{eL}^{+} and θ_{eM}^{+} in buoyancy as expected from (17).

To measure $\frac{\delta\theta_{eM}^{+}}{\delta\theta_{eL}^{+}}$, we first shift all the onset curves in Figure 3a such that they reach a pre-determined threshold value of precipitation (0.95 mm/hr in this case) at the same value of θ_{eL}^{+}. This threshold was empirically chosen to give the best overlap of the precipitation onset curves. The near collapse of the curves in Figure 3b is encouraging since it suggests that a single function of buoyancy can describe the behavior of conditionally averaged tropical precipitation. The average of these curves is shown in Figure 3c; the slope of the steepest part of this average onset curve is extended to zero precipitation to estimate a critical value of θ_{eL}^{+} for which the precipitation strongly picks up. The critical value of pickup for each of the curves in Figure 3a is then estimated by simply adding their respective linear shifts to the critical value estimated for the average pickup curve. This critical value θ_{eLC}^{+} signifies the approximate θ_{eL}^{+} value at which precipitation onset occurs for each of the curves in Figure 3a. Figure 3d shows the shifts in θ_{eL}^{+} in response to changing θ_{eM}^{+} values exhibiting a linear relationship and yielding an estimate of -1.03 for the slope $\frac{\delta\theta_{eL}^{+}}{\delta\theta_{eM}^{+}}$ and therefore $-\frac{c\Delta p_M}{b\Delta p_L}$. In principle, this shift procedure could detect a nonlinear dependence in which the slope varied as a function of θ_{eM}^{+}, but the emergence of the linear relationship here is consistent with the linear dependence derived under the assumptions of (17), at least within the range of variations in θ_{eL}^{+} and θ_{eM}^{+} considered here.

A similar procedure is shown in Figure 4, where θ_{eM}^{+} and θ_{ed}^{*} are held roughly constant and the boundary layer component θ_{eBL} is allowed to vary relative to θ_{eL}^{+}. In this case, $\frac{\delta\theta_{eL}^{+}}{\delta\theta_{eBL}} = \frac{a\Delta p_B}{b\Delta p_L} \sim 0.88$ is estimated from the linear shifts, using a precipitation threshold of .7 mm/hr to produce a good collapse. Using these two relative weights and with the knowledge that M(p_F) is $a_p\Delta p_B + b_p\Delta p_L + c_p\Delta p_M$, we estimate values for $\frac{a\Delta p_B}{M(p_F)}$ (= 0.30), $\frac{b\Delta p_L}{M(p_F)}$ (= 0.35) and $\frac{c\Delta p_M}{M(p_F)}$ (= 0.35). Note that these values are the coefficients in (17) that can be used to compute the freezing level buoyancy B_F. Physically, *these relative weightings quantify the influence of each layer to the plume buoyancy at the freezing level*. In this reverse-engineered inflow profile, the contribution from each of the free tropospheric layers is nearly the same, with a slightly smaller contribution from the boundary layer. This inflow profile, i.e. the piecewise mass-flux profile using the weights derived here, is displayed in Figure 1b for a unit mass-flux at the freezing level. The overall result implies a relatively uniform increase in mass flux with height, i.e. a deep inflow, corresponding to a relatively uniform weighting of the contributions of each layer to freezing level buoyancy.

We also test the sensitivity of the estimated weights to details of the binning procedure such as the values of the variables being held constant and the bin resolution of the variables. Changes in these parameters do produce variations in the computed weightings and the resulting influence function, but they do not greatly impact our final results. Figures 5 and 6, illustrate these cases. Figure 5 presents a case where a variant in the procedure results in a slight change in the weightings, showing the precipitation onset for increases in θ_{eBL} instead of decreases in θ_{eL}^{+}; the bin resolution is 0.5 K for θ_{eBL} and 2 K for the other variables. In Figure 5, θ_{eM}^{+} and θ_{ed}^{*} are held constant, while allowing θ_{eBL} and θ_{eL}^{+} to change. Increases in the boundary layer θ_{eBL} results in precipitation onset beyond an apparent threshold value with the onset occurring for smaller θ_{eBL} values in a lower troposphere closer to saturation, consistent with our buoyancy-based framework. With a precipitation threshold of 0.75 mm/hr, a linear shifting procedure, as before, yields a weighting of ~0.79 for $\frac{\delta\theta_{eBL}}{\delta\theta_{eL}^{+}} = \frac{b\Delta p_L}{a\Delta p_B}$, in contrast to the expected $(.88)^{-1} = 1.13$ from Figure 4.

In Figure 6, we present the precipitation onset with θ_{eL}^{+} and θ_{ed}^{*} held constant, but with varying θ_{eM}^{+} and θ_{eBL}. The resultant weighting for $\frac{\delta\theta_{eBL}}{\delta\theta_{eM}^{+}} = \frac{c\Delta p_M}{a\Delta p_L}$ is ~ 0.75,

which yields $\frac{c\Delta p_M}{b\Delta p_L}$ ~1.05, very close to the estimate from Figure 4. The precipitation threshold for this shifting exercise was 0.5 mm/hr. Figures 5 and 6 therefore illustrate the expected range of variability from changing the bin resolution. The relative weights of the two free tropospheric layers remains nearly the same as before, but the weighting from the boundary layer has increased. This new weighting yields the following values for the layer weights: $\frac{a\Delta p_B}{M(p_F)}$ (= 0.39), $\frac{b\Delta p_L}{M(p_F)}$ (= 0.31) and $\frac{c\Delta p_M}{M(p_F)}$ (= 0.3). These values correspond to an inflow profile that weights the boundary layer slightly more than the free tropospheric layers. Because the weightings remain similar among layers, however, the overall result of implying a deep inflow remains.

4.4 Free tropospheric temperature dependence

We have thus far utilized the hypothesis that variations in freezing level buoyancy (B_F) capture variations in precipitation onset to derive the layer influence function. The weights derived in the previous section will be used in section 5 to test whether the integrated buoyancy (B_{int}) yields a sharp onset profile. It is worth first asking if B_F by itself is enough to predict the precipitation onset under all conditions. If this were the case, then increases in free tropospheric temperature value (θ_{ed}^*) should result in increased values of B_F, i.e. a data-derived estimate for d, should at least be positive and close to $b\Delta p_L + c\Delta p_M$. In Figure 7, we present a similar sequence of figures as in Figures 3-6, but now holding θ_{eM}^+ (4 K bins) and θ_{eBL} (2 K bin width) constant and allowing critical θ_{eL}^+ to shift as a function of the deep tropospheric temperature (θ_{ed}^*). We find that the precipitation picks up at a higher value of θ_{eLT}^+ for colder tropospheric temperatures, yielding a negative value for $\frac{d}{b\Delta p_L}$ (-0.82). This implies that a warmer troposphere (compared to the freezing level temperature) requires a lower troposphere closer to saturation for precipitation onset. The negative sign is robust to the variations in the parameters like bin resolution, values being held constant etc. (not shown). This variation of the precipitation onset curve to changing free tropospheric temperatures therefore suggests *that the utility of B_F as a predictor of conditional precipitation is limited to environmental variations not involving the free tropospheric temperature.* This allows to modify our earlier $< P >$ vs B_F postulate and rewrite it as:

$$< P >= f(B_F)\Big|_{\theta_{ed}^*} \tag{18}$$

indicating that the hypothesis linking conditional precipitation and B_F is valid in the presence of invariant deep tropospheric temperature variations. One possible reason for this relationship is that increased temperature at lower levels can cause local decreases in

buoyancies even if (17) yields increasing buoyancies at the freezing level. The layer influence function, however, can be deduced from the moisture variations alone, while holding the magnitude of the deep temperature structure constant, as in the shifting procedures described in Figures 3-6. It is the simple analytical form for B_F given in (16) and (17) that facilitates this deduction. B_{int}, which is a bulk estimate of the lower-tropospheric buoyancy is postulated to be a more robust predictor of precipitation onset under varying environmental conditions.

5. The precipitation-buoyancy relationship

The layer weightings obtained from the shifting operations using B_F are used to estimate B_{int}. This section tests the relationship between B_{int} estimated in this manner—over both tropical land and ocean—and conditional precipitation across both land and ocean in the tropics. In other words, we ask if $< P >= f(B_{\text{int}})$ is a valid hypothesis governing the behavior of tropical precipitation.

As background for evaluation in θ_e variables, Figure 8 shows the precipitation onset curves using the previously used bulk measures of CWV and $\hat{T}$, calculated over seven tropical land regions and compared to the curve from the tropical Western Pacific. When categorized by these traditional bulk thermodynamic variables, the precipitation still shows a strong increase with CWV over land, but the onset occurs at smaller CWV values over land than ocean. Some of these differences are attributable to orographic precipitation—as measured by surface pressure. When the land and ocean points with similar values of surface pressure are used in the analysis, the land-ocean differences are less stark (see Supplement, Figure S5). It would, however, be theoretically satisfying if we can reconcile the land-ocean differences or even reproduce the precipitation onset curves from Figure 8 using a single variable representative of buoyancy.

We take as our sole variable representative of buoyancy the empirically determined, θ_e-based buoyancy, B_{int}, computed using the reverse engineered inflow profile from Section 5. Among the slight variants of the inflow profiles, based on the details of the binning and shifting procedures noted in Section 5, we choose the profile reconstructed from Figures 3 and 4 ($\frac{a\Delta p_B}{M(p_F)} = 0.30$, $\frac{b\Delta p_L}{M(p_F)} = 0.35$ and $\frac{c\Delta p_M}{M(p_F)} = 0.35$). After substituting for coefficients A-E in (15) and calculating the other layer averaged thermodynamic variables from the reanalysis data, we can compute B_{int} for any given thermodynamic profile.

Figure 9 shows the precipitation binned against B_{int}, for the four ocean basins as well as the land regions. Figure 9a shows that B_{int} is able to capture the onset of averaged precipitation over all tropical oceans. Among many encouraging features in Figure 9 is the sharp onset in precipitation as a function of this measure of buoyancy, with positive values of B_{int} associated with strong precipitation. Note that the y-axis in Figure 9a

extends to 5 mm/hr, much higher than the largest precipitation seen when binned by CWV and $\hat{T}$, indicative of an even stronger relationship in terms of B_{int}. We note that the sharp increase in precipitation begins at slightly negative values of buoyancy, as will be discussed further below.

Figure 9b and 9c show how the land precipitation curves onset at nearly the same B_{int} values as the oceanic curves, with sharp pickups that are generally comparable through the main part of the onset. We note again that the coefficients established empirically over the ocean are used here for the continental regions. There are some discrepancies between the land and ocean curves, with the land curves typically not attaining as large precipitation values for high values of B_{int}, especially for the highly precipitating and sparsely sampled points, where the land regions of South American (S.Amer), Maritime Continent (M.Cont) and Argentia (Arg) become rather noisy. For West Africa (W.Afr) and India, the precipitation curves seem to attain onset at slightly higher values than the ocean, while Arg and S.Amer seem to do so at slightly lower values. Despite these minor differences, the striking nature of the land-ocean collapse using B_{int} and the sharpness of the pickup is taken to support our conjecture relating precipitation onset to an integrated buoyancy measure in the lower free troposphere. Even more encouraging is that the use of a single reverse-engineered inflow profile from over the tropical oceans is able to capture the precipitation onset over tropical land as well. This implies that the deep inflow profile is a useful conceptual tool to describe salient features of convection-environmental interactions across the tropical world.

Figure 10 shows the probability density function (PDF) for B_{int}, much like the convective transition statistics generally presented for CWV (e.g. Neelin et al. 2009, Kuo et al. 2017). Like CWV, B_{int} shows sharply peaked distribution close to precipitation onset for both precipitating (Figure 10a) and total points (Figure 10b), at 0 m/s^2, for all regions. Here 0.25 mm/hr is used as the threshold to identify precipitating points. Another universal feature of the PDF is the sharp drop in the occurrence frequency of positive B_{int} values just beyond the precipitation onset for all regions. The nearly identical distributions between B_{int} and CWV (see Figure 5 in Neelin et al. 2009) suggest that CWV does indeed control much of the variation in free tropospheric buoyancy as supposed earlier (e.g. in HN09). The PDF of B_{int} shown in Figure 10 suggest that precipitation acts to reduce positive excursions in grid-scale buoyancy—whose mean value is presumably set by a combination of radiative and lateral transport of heat and moisture. This is one manifestation of convective quasi-equilibrium (Arakawa and Schubert 1974) where the environmental buoyancy is destabilized by slowly-varying environmental processes and stabilized by rapid increases in precipitation; with the system self-modulated by the convective-circulation ensemble, as proposed in Peters and Neelin (2006).

There is a high incidence of precipitating points over East Asia (E.Asia) for low values of B_{int} in Figure 10b. This feature disappears when only the active monsoon

months (June-September) are considered (not shown); this indicates that the precipitating points at low B_{int} values might represent wintertime frontal precipitation. This is also true for Australia (Aus) and Argentina, where the long precipitating tail at low B_{int} values is reduced when only considering austral summertime precipitation. We nevertheless retain all times of the year in our analysis as it bolsters the sampling; the artifacts from the frontal precipitation regime are only noticeable in the weakly precipitating regime.

6. Discussion

6.1 Convective transition statistics in θ_e-based variables

In this study, we introduce a framework to relate precipitation to the environmental buoyancy. We present two buoyancy measures (B_F and B_{int}) that are dependent on the vertical thermodynamic structure through an empirically determined inflow—or a layer influence—profile. The inflow profile was estimated by positing a link between the conditional precipitation over tropical ocean and the freezing level buoyancy, B_F, which we found was a useful working hypothesis in the absence of free tropospheric variations.

To account for a more complete relationship between conditional precipitation and the environment, we computed B_{int}, using the layer weights estimated through B_F. The collapse of the precipitation onset using B_{int} across a variety of tropical environments—particularly the land and ocean—provides a strong indicator that this quantity can capture leading behavior of precipitation-producing convection.

B_{int} is calculated in a θ_e-based variable space, with the saturation equivalent potential temperature θ_e^* and the subsaturation, θ_e^+, playing the role of temperature and moisture respectively. The use of B_{int} is appealing for a number of reasons: dependence on lower tropospheric thermodynamic information is consistent with the need for updrafts to be buoyant through this layer to reach deep convective status, and with high-resolution modeling results demonstrating that convection is sensitive to perturbations in this layer (Tulich and Mapes 2010, Kuang 2010, Wang and Sobel 2012); the dominant relationship can be sought without complexity of freezing microphysics effects; furthermore, this buoyancy can be linked naturally to an updraft form that sidesteps some unnecessary complications of parcel lifting paradigms.

As discussed in the Introduction, the importance of the free tropospheric water vapor to convection has been strongly emphasized in literature. Water vapor, however, must be placed in context with respect to its importance to the buoyancy—which is a stronger diagnostic measure of tropical convection fueled by the release of convective instability. The land-ocean differences in the precipitation-moisture relationship and their unification in buoyancy space (Figures 9 and 10) underscores this point. Water vapor therefore only emerges as the leading order variable, when the other implicit controls such as the boundary layer moist entropy and free-tropospheric stability (Back and

Bretherton 2009, Raymond and Flores 2016) are (relatively) unchanging. When making statements about buoyancy in presence of strong entrainment effects, however, the key question is how to quantify the dependence of buoyancy on the environment as a function of height.

6.2 Empirical estimation of inflow profiles

Most mass-flux based cumulus parameterization schemes deduce the cloud or cloud-ensemble mass flux from an assumed value of the fractional entrainment that is ultimately used to predict the precipitation. In this study, we solve the parameterization problem in reverse, asking what is the entrainment profile that yields a collapse of the observed precipitation onset across the tropics. Here entrainment is estimated in terms of a deep inflow of environmental air that enters the plume at every level from the surface up until the freezing level. In the cumulus parameterization analogy, our closure postulate is the linkage of conditional-average precipitation to the integrated buoyancy in the lower troposphere. Having derived the dependence of buoyancy on mass inflow, we proceed to estimate the inflow profile that yields a universal dependence on the resulting buoyancy. Our reverse-engineered deep inflow profile, depicted in Figure 1b, shows a steady increase in the mass-flux from zero at the surface. The magnitude of the inflow weights the influence of the environment in each layer. It is notable that the shape of this inflow profile is nearly unchanging for variations in environmental thermodynamic values (note the nearly linear variations shown in Figures 4-7). The use of a single inflow profile is further supported by the collapse of the precipitation statistics over tropical land in line with the tropical ocean statistics.

The result that a single inflow profile captures leading behavior of the convection-environmental interactions also has some bearing on the entrainment assumptions usually employed in cumulus parameterization schemes. One class of schemes argues for the use of constant mixing with height (as implemented in Arakawa and Schubert 1974; Kain and Fritsch 1990; Zhang and McFarlane 1995 etc.). Other arguments have sought to introduce some vertical variation of the mixing coefficient with height, by linking the entrainment to the production of buoyant kinetic energy (Lin 1999; Gregory 2001; Jensen and Del Genio 2006, de Rooy and Siebesma 2010). Our results suggest that a fixed, judiciously chosen weighting, corresponding to a vertically varying entrainment inflow profile is effective in reproducing the onset to deep convection. The use of a fixed inflow profile also sidesteps the pitfalls associated with the assumptions made in a more interactive plume model involving the steady-state plume vertical velocity equation (de Roode et al. 2012).

Our framework works with the integral form of the traditional bulk plume equation (3), in contrast to studies working with the differential entraining plume equation (5). This gives our framework a slightly different physical interpretation than those imposing entraining plume assumptions. Our framework stresses the importance of the influence function (2) in affecting the plume buoyancy, while traditional entraining

plume studies stress the importance of the mixing coefficient. These two interpretations are mathematically equivalent within the framework of a well-mixed plume, although if the plume is not instantly mixed at each level, the integral formulation would tend to be more robust. For instance, the entrainment formulations obtained from studies of shallow convection (Siebesma 1996; Jakob and Siebesma 2003; Bretherton et al. 2004a, Siebesma et al. 2007) yield values that scale inversely with height. This 1/z –like profile can also be obtained if one were to invert our linear deep inflow profile to yield the entrainment coefficient. Notice however, that the physical interpretation for the existence of the 1/z-like profile is quite different in the two cases. The shallow convection studies invoke the eddy mixing length scale argument (Siebesma 1996), while we base our deep inflow profile on tropical vertical velocity and mass-flux observations.

Some recent idealized simulations (Romps 2010, Dawe and Austin 2011, Yeo and Romps 2013) have found that actual entrainment values in clouds may be much higher than values usually used in bulk-plume schemes and that it may be useful to distinguish between entrainment and updraft dilution (Hannah 2017). The high entrainment values obtained in these studies appear to depend on the fact that actual clouds entrain not only clear-air but also detritus from themselves and other clouds. These studies raise interesting questions about how to transfer information to the idealized world of cumulus parameterization, but also highlight the utility of using the influence function to understand environmental interaction with the plume. Our influence function subsumes the subgrid-scale interactions between the plume and the environment, yielding an estimation of only the bulk effects. As such, it directly addresses the parameterization problem for the linkage between the environmental θ_e and precipitation. Errors in our formulation, which interprets the influence function in terms of dynamical entrainment alone would affect the details of the inferred mass flux in Figure 1. However, the influence function itself would remain empirically valid for representing the bulk effects of strongly precipitating tropical convection over a variety of environments.

6.3 Caveats and unaddressed effects:

Our framework does not account for more complex—and perhaps higher-order—variations in tropical convection. The single, universal B_{int} measure gives slightly imperfect collapse between land and ocean onset curves, with considerable scatter at high B_{int} values. This scatter is a potential artifact of errors in the data source or could represent the myriad factors that confound the study of continental precipitation such as soil moisture content (Betts et al. 1996, Emori 1998, Spracklen et at. 2012), orography (Houze 2012; Shige and Kummerow 2016) and more prominently, the daytime heating that produces a prominent diurnal cycle (Nesbitt and Zipser 2003, Kikuchi and Wang 2008). Even though we implicitly capture parts of these effects (for e.g. the diurnal cycle and soil moisture effects using the boundary layer θ_e values, orography using a sigma-like coordinate system) we still ignore other features like diurnal variations in the boundary layer height.

Note that our buoyancy definition in (8) excludes the virtual temperature effects, which could potentially have sizeable impacts for the weakly precipitating points (Doswell and Rasmussen, 1994). Another source of discrepancy between the land and ocean onset curves, not included in the present framework is the explicit distinction between convective and stratiform precipitation (Houze 1997, Schumacher and Houze 2003). Stratiform rain is more extensive over tropical oceans than tropical land (Houze et al. 2015) and its occurrence is not solely governed by buoyancy considerations. A more direct measure relating environmental parameters to stratiform rain could potentially resolve some of the discrepancy between tropical land and ocean onset curves, particularly at the high B_{int} values, seen in Figure 9.

7. Conclusions with Implications

We present a framework to understand the strong relationship between bulk tropospheric temperature and moisture variables with tropical precipitation and capture the observed variability in this relationship. This framework relates the buoyancy of a plume directly to layer averages of the appropriate thermodynamic variables below the freezing level, under the assumption that the environment influences the plume throught a deep inflow mass-flux profile. The deep inflow mass-flux profile was deduced from observations and was used to compute a measure of integrated buoyancy in the lower free-troposphere (B_{int}). B_{int} is an effective predictor of the onset in precipitation across different regimes in the tropics—both land and ocean—despite patent differences in their respective environmental conditions. The method used to reverse engineer the deep inflow mass-flux here relies on the availability of large amounts of data. This method is an example of a hypothesis-based effort to probe large datasets, in contrast to big data machine-learning methods that are finding greater use in earth sciences.

Convective transition statistics, being a rather robust property of tropical convection, have great utility in diagnosing GCMs (Kuo et al. 2017). B_{int} is an inflow-dependent property of convection, similar in form to measures of integrated buoyancy (cloud work function in Arakawa and Schubert 1974; CAPE in Zhang and McFarlane 1995; Bechtold et al. 2000 etc.) generally used to treat the closure problem in parameterization schemes. The set of convective transition statistics involving B_{int} shown in Figures 9 and 10 should therefore be a useful target of future GCM and cumulus parameterization diagnostics. Other interesting diagnostic exercises with GCMs can involve reverse engineering the model's precipitation onset (as in Figures 3-7) to understand the influence function that governs the transition to deep convection in the model relative to that estimated from observations.

The ability of a simple measure like B_{int} to predict convective transition statistics without the inclusion of ice-phase physics and other intricate microphysics schemes bodes well for cumulus parameterization schemes, though land-ocean differences at higher precipitation rates might show dependence on the microphysics. B_{int} does not explicitly include triggering mechanisms such as surface eddies (given by surface

turbulent kinetic energy), cold pools or gravity waves. An interesting feature of the precipitation-buoyancy relationship is the sharp increase in precipitation for slightly negative B_{int} values. This onset at negative B_{int} could point to buoyancy sources unaccounted by B_{int}, which could potentially include triggers. For instance, the dynamic triggering of convection by cold pools (Jevanjee and Romps 2015) would not be accounted for in our purely thermodynamic view of buoyancy. The robustness of the precipitation-buoyancy relationship across the tropics, however, suggests they can be treated in a general framework.

Lastly, in quantifying the utility of the vertical thermodynamic structure, three layer-averages in the lower troposphere are found adequate to capture the precipitation statistics. This finding is anticipated to find synergy with future observational efforts to partially resolve remotely sensed thermodynamic data in the vertical (Wulfmeyer et al. 2015). We expect that a few coarsely resolved layers of the lower troposphere could help observationally constrain key environmental predictors of precipitation statistics in the tropics.

Acknowledgements

We would like to thank Kathleen Schiro, Roger Smith and two anonymous reviewers for useful feedback on this manuscript. This research was supported in part by National Science Foundation Grant AGS-1505198, National Oceanic and Atmospheric Administration Grants NA14OAR4310274 and NA15OAR4310097.

References

Ahmed, F., and C. Schumacher, 2015: Convective and stratiform components of the precipitation-moisture relationship. *Geophysical Research Letters*, **42**.

——, 2017: Geographical differences in the tropical precipitation-moisture relationship and rain intensity onset. *Geophysical Research Letters*, **44,** 1114-1122.

Allen, T. L. and Mapes, B. E. (2017), The late spring Caribbean rain-belt: climatology and dynamics. Int. J. Climatol. doi:10.1002/joc.5136

Arakawa, A. and W.H. Schubert, 1974: Interaction of a Cumulus Cloud Ensemble with the Large-Scale Environment, Part I. *J. Atmos. Sci.,* **31**, 674–701,https://doi.org/10.1175/1520-0469(1974)031<0674:IOACCE>2.0.CO;2

Asai, T. and A. Kasahara, 1967: A Theoretical Study of the Compensating Downward Motions Associated with Cumulus Clouds. *J. Atmos. Sci.,* **24**, 487–496,https://doi.org/10.1175/1520-0469(1967)024<0487:ATSOTC>2.0.CO;2

Back, L. E., and C. S. Bretherton, 2009: On the Relationship between SST Gradients, Boundary Layer Winds, and Convergence over the Tropical Oceans. *Journal of Climate*, **22,** 4182-4196.

Betts, A. K., 1975: Parametric interpretation of trade-wind cumulus budget studies. *Journal of the Atmospheric Sciences*, **32,** 1934-1945.

Betts, A. K., J. H. Ball, A. C. M. Beljaars, M. J. Miller, and P. A. Viterbo, 1996: The land surface-atmosphere interaction: A review based on observational and global modeling perspectives. *Journal of Geophysical Research-Atmospheres*, **101,** 7209-7225.

Bretherton, C. S., M. E. Peters, and L. E. Back, 2004a: Relationships between water vapor path and precipitation over the tropical oceans. *Journal of Climate*, **17,** 1517-1528.

Bretherton, C. S., J. R. McCaa, and H. Grenier, 2004b: A new parameterization for shallow cumulus convection and its application to marine subtropical cloud-topped boundary layers. Part I: Description and 1D results. *Monthly Weather Review*, **132,** 864-882.

Chaboureau, J. P., F. Guichard, J. L. Redelsperger, and J. P. Lafore, 2004: The role of stability and moisture in the diurnal cycle of convection overland. *Quarterly Journal of the Royal Meteorological Society*, **130,** 3105-3117.

Dawe, J. T., and P. H. Austin, 2011: The Influence of the Cloud Shell on Tracer Budget Measurements of LES Cloud Entrainment. *Journal of the Atmospheric Sciences*, **68,** 2909-2920.

de Roode, S. R., A. P. Siebesma, H. J. J. Jonker, and Y. de Voogd, 2012: Parameterization of the Vertical Velocity Equation for Shallow Cumulus Clouds. *Monthly Weather Review*, **140,** 2424-2436.

de Rooy, W. C., and A. P. Siebesma, 2010: Analytical expressions for entrainment and detrainment in cumulus convection. *Quarterly Journal of the Royal Meteorological Society*, **136,** 1216-1227.

de Rooy, W. C., and Coauthors, 2013: Entrainment and detrainment in cumulus convection: an overview. *Quarterly Journal of the Royal Meteorological Society*, **139,** 1-19.

Dee, D. P., and Coauthors, 2011: The ERA-Interim reanalysis: configuration and performance of the data assimilation system. *Quarterly Journal of the Royal Meteorological Society*, **137,** 553-597.

Del Genio, A. D., and J. B. Wu, 2010: The Role of Entrainment in the Diurnal Cycle of Continental Convection. *Journal of Climate*, **23,** 2722-2738.

Del Genio, A. D., Y. H. Chen, D. Kim, and M. S. Yao, 2012a: The MJO Transition from Shallow to Deep Convection in CloudSat/CALIPSO Data and GISS GCM Simulations. *Journal of Climate*, **25,** 3755-3770.

Del Genio, A. D., 2012b: Representing the Sensitivity of Convective Cloud Systems to Tropospheric Humidity in General Circulation Models. *Surveys in Geophysics*, **33,** 637-656.

Derbyshire, S. H., I. Beau, P. Bechtold, J. Y. Grandpeix, J. M. Piriou, J. L. Redelsperger, and P. M. M. Soares, 2004: Sensitivity of moist convection to environmental humidity. *Quarterly Journal of the Royal Meteorological Society*, **130,** 3055-3079.

Doswell, C. A., and E. N. Rasmussen, 1994: The effect of neglecting the virtual temperature correction on cape calculations. *Weather and Forecasting*, **9,** 625-629.

Emori, S., 1998: The interaction of cumulus convection with soil moisture distribution: An idealized simulation. *Journal of Geophysical Research-Atmospheres*, **103,** 8873-8884.

Ferrier, B. S., and R. A. Houze, 1989: One-dimensional time-dependent modeling of gate cumulonimbus convection. *Journal of the Atmospheric Sciences*, **46,** 330-352.

Gregory, D., 2001: Estimation of entrainment rate in simple models of convective clouds. *Quarterly Journal of the Royal Meteorological Society*, **127,** 53-72.

Hannah, W. M., and E. D. Maloney, 2011: The Role of Moisture-Convection Feedbacks in Simulating the Madden-Julian Oscillation. *Journal of Climate*, **24,** 2754-2770.

Hannah, W. M., B. E. Mapes, and G. S. Elsaesser, 2016: A Lagrangian View of Moisture Dynamics during DYNAMO. *Journal of the Atmospheric Sciences*, **73,** 1967-1985.

Hannah, W.M., 2017: Entrainment vs. Dilution in Tropical Deep Convection. *J. Atmos. Sci.,* **0**, https://doi.org/10.1175/JAS-D-16-0169.1

Holloway, C. E., and J. D. Neelin, 2009: Moisture Vertical Structure, Column Water Vapor, and Tropical Deep Convection. *Journal of the Atmospheric Sciences*, **66,** 1665-1683.

Hou, A. Y., and Coauthors, 2014: The global precipitation measurement mission. *Bulletin of the American Meteorological Society*, **95,** 701-+.

Houghton, H. G., and H. E. Cramer, 1951: A theory of entrainment in convective currents. *Journal of Meteorology*, **8,** 95-102.

Houze, R. A., 1997: Stratiform precipitation in regions of convection: A meteorological paradox? *Bulletin of the American Meteorological Society*, **78,** 2179-2196.

Houze, R. A., 2004: Mesoscale convective systems. *Reviews of Geophysics*, **42,** 43.

——, 2012: Orographic effects on precipitating clouds. *Reviews of Geophysics*, **50**.

Houze, R. A., Jr., K. L. Rasmussen, M. D. Zuluaga, and S. R. Brodzik, 2015: The variable nature of convection in the tropics and subtropics: A legacy of 16years of the Tropical Rainfall Measuring Mission satellite. *Reviews of Geophysics*, **53,** 994-1021.

Huffman, G. J., and Coauthors, 2007: The TRMM multisatellite precipitation analysis (TMPA): Quasi-global, multiyear, combined-sensor precipitation estimates at fine scales. *Journal of Hydrometeorology*, **8,** 38-55.

Jakob, C., and A. P. Siebesma, 2003: A new subcloud model for mass-flux convection schemes: Influence on triggering, updraft properties, and model climate. *Monthly Weather Review*, **131,** 2765-2778.

Jensen, M. P., and A. D. Del Genio, 2006: Factors limiting convective cloud-top height at the ARM Nauru Island climate research facility. *Journal of Climate*, **19,** 2105-2117.

Jeevanjee, N., and D. M. Romps, 2015: Effective Buoyancy, Inertial Pressure, and the Mechanical Generation of Boundary Layer Mass Flux by Cold Pools. *Journal of the Atmospheric Sciences*, **72,** 3199-3213.

Kain, J. S., and J. M. Fritsch, 1990: A one-dimensional entraining detraining plume model and its application in convective parameterization. *Journal of the Atmospheric Sciences*, **47,** 2784-2802.

Kikuchi, K., and B. Wang, 2008: Diurnal precipitation regimes in the global tropics. *Journal of Climate*, **21,** 2680-2696.

Kingsmill, D. E., and R. A. Houze, 1999: Thermodynamic characteristics of air flowing into and out of precipitating convection over the west Pacific warm pool. *Quarterly Journal of the Royal Meteorological Society*, **125,** 1209-1229.

Kuang, Z. M., 2008: A moisture-stratiform instability for convectively coupled waves. *Journal of the Atmospheric Sciences*, **65,** 834-854.

——, 2010: Linear Response Functions of a Cumulus Ensemble to Temperature and Moisture Perturbations and Implications for the Dynamics of Convectively Coupled Waves. *Journal of the Atmospheric Sciences*, **67,** 941-962.

Kumar, V. V., C. Jakob, A. Protat, C. R. Williams, and P. T. May, 2015: Mass-Flux Characteristics of Tropical Cumulus Clouds from Wind Profiler Observations at Darwin, Australia. *Journal of the Atmospheric Sciences*, **72,** 1837-1855.

Kuo, Y. H., J. D. Neelin, and C. R. Mechoso, 2017: Tropical Convective Transition Statistics and Causality in the Water Vapor-Precipitation Relation. *Journal of the Atmospheric Sciences*, **74,** 915-931.

Lemone, M. A., and E. J. Zipser, 1980: Cumulonimbus Vertical Velocity Events In Gate .1. Diameter, Intensity And Mass Flux. *Journal of the Atmospheric Sciences*, **37,** 2444-2457.

Lin, C. C., 1999: Some bulk properties of cumulus ensembles simulated by a cloud-resolving model. Part II: Entrainment profiles. *Journal of the Atmospheric Sciences*, **56,** 3736-3748.

Mapes, B. E., and R. A. Houze, 1995: di[abatic divergence profiles in western pacific mesoscale convective systems. *Journal of the Atmospheric Sciences*, **52,** 1807-1828.

Martin, S. T., and Coauthors, 2016: Introduction: Observations and Modeling of the Green Ocean Amazon (GoAmazon2014/5). *Atmospheric Chemistry and Physics*, **16,** 4785-4797.

Masunaga, H., and Z. J. Luo, 2016: Convective and large-scale mass flux profiles over tropical oceans determined from synergistic analysis of a suite of satellite observations. *Journal of Geophysical Research-Atmospheres*, **121,** 7958-7974.

Mechem, D. B., R. A. Houze, and S. S. Chen, 2002: Layer inflow into precipitating convection over the western tropical Pacific. *Quarterly Journal of the Royal Meteorological Society*, **128,** 1997-2030.

Morrison, H., 2017: An Analytic Description of the Structure and Evolution of Growing Deep Cumulus Updrafts. *J. Atmos. Sci.,* **74**, 809–834, https://doi.org/10.1175/JAS-D-16-0234.1

Morton, B. R., G. Taylor, and J. S. Turner, 1956: Turbulent gravitational convection from maintained and instantaneous sources. *Proceedings of the Royal Society of London Series a-Mathematical and Physical Sciences*, **234,** 1-+.

Myoung, B., and J. W. Nielsen-Gammon, 2010: Sensitivity of Monthly Convective Precipitation to Environmental Conditions. *Journal of Climate*, **23,** 166-188.

Neale, R. B., J. H. Richter, and M. Jochum, 2008: The Impact of Convection on ENSO: From a Delayed Oscillator to a Series of Events. *Journal of Climate*, **21,** 5904-5924.

Neelin, J. D., O. Peters, and K. Hales, 2009: The Transition to Strong Convection. *Journal of the Atmospheric Sciences*, **66,** 2367-2384.

Neelin, J. D., O. Peters, J. W. B. Lin, K. Hales, and C. E. Holloway, 2008: Rethinking convective quasi-equilibrium: observational constraints for stochastic convective schemes in climate models. *Philosophical Transactions of the Royal Society a-Mathematical Physical and Engineering Sciences*, **366,** 2581-2604.

Nesbitt, S. W., and E. J. Zipser, 2003: The diurnal cycle of rainfall and convective intensity according to three years of TRMM measurements. *Journal of Climate*, **16,** 1456-1475.

Pandya, R. E., and D. R. Durran, 1996: The influence of convectively generated thermal forcing on the mesoscale circulation around squall lines. *Journal of the Atmospheric Sciences*, **53,** 2924-2951.

Peters, O., and J. D. Neelin, 2006: Critical phenomena in atmospheric precipitation. *Nature Physics*, **2,** 393-396.

Peters, O., J. D. Neelin, and S. W. Nesbitt, 2009: Mesoscale Convective Systems and Critical Clusters. *Journal of the Atmospheric Sciences*, **66,** 2913-2924.

Prigent, C., F. Aires, and W. B. Rossow, 2006: Land surface microwave emissivities over the globe for a decade. *Bulletin of the American Meteorological Society*, **87,** 1573

Raymond, D. J., 2000: Thermodynamic control of tropical rainfall. *Quarterly Journal of the Royal Meteorological Society*, **126,** 889-898.

Raymond, D. J., and M. M. Flores, 2016: Predicting convective rainfall over tropical oceans from environmental conditions. *Journal of Advances in Modeling Earth Systems*, **8,** 703-718.

Redelsperger, J. L., D. B. Parsons, and F. Guichard, 2002: Recovery processes and factors limiting cloud-top height following the arrival of a dry intrusion observed during TOGA COARE. *Journal of the Atmospheric Sciences*, **59,** 2438-2457.

Romps, D. M., 2010: A Direct Measure of Entrainment. *Journal of the Atmospheric Sciences*, **67,** 1908-1927.

Romps, D. M., and Z. M. Kuang, 2011: A Transilient Matrix for Moist Convection. *Journal of the Atmospheric Sciences*, **68,** 2009-2025.

Sahany, S., J. D. Neelin, K. Hales, and R. B. Neale, 2012: Temperature-Moisture Dependence of the Deep Convective Transition as a Constraint on Entrainment in Climate Models. *Journal of the Atmospheric Sciences*, **69,** 1340-1358.

Schiro, K. A., J. D. Neelin, D. K. Adams, and B. R. Lintner, 2016: Deep Convection and Column Water Vapor over Tropical Land versus Tropical Ocean: A Comparison between the Amazon and the Tropical Western Pacific. *Journal of the Atmospheric Sciences*, **73,** 4043-4063.

Schiro, K.A, 2017: Thermodynamic controls on deep convection in the tropics: observations and applications to modeling, University of California, Los Angeles, 148 pp.

Schumacher, C., and R. A. Houze, 2003: Stratiform rain in the tropics as seen by the TRMM precipitation radar. *Journal of Climate*, **16,** 1739-1756.

Schumacher, C., S. N. Stevenson, and C. R. Williams, 2015: Vertical motions of the tropical convective cloud spectrum over Darwin, Australia. *Quarterly Journal of the Royal Meteorological Society*, **141,** 2277-2288.

Sherwood, S. C., 1999: Convective precursors and predictability in the tropical western Pacific. *Monthly Weather Review*, **127,** 2977-2991.

Sherwood, S. C., P. Minnis, and M. McGill, 2004: Deep convective cloud-top heights and their thermodynamic control during CRYSTAL-FACE. *Journal of Geophysical Research-Atmospheres*, **109**.

Shige, S., and C. D. Kummerow, 2016: Precipitation-Top Heights of Heavy Orographic Rainfall in the Asian Monsoon Region. *Journal of the Atmospheric Sciences*, **73,** 3009-3024.

Siebesma, P., 1996: On the mass flux approach for atmospheric convection, Workshop on New Insights and Approaches to Convective Parametrization, 4-7 November 1996 (Shinfield Park, Reading), ECMWF, ECMWF, 1996, pp. 25–57.

Siebesma, A. P., P. M. M. Soares, and J. Teixeira, 2007: A combined eddy-diffusivity mass-flux approach for the convective boundary layer. *Journal of the Atmospheric Sciences*, **64,** 1230-1248.

Spracklen, D. V., S. R. Arnold, and C. M. Taylor, 2012: Observations of increased tropical rainfall preceded by air passage over forests. *Nature*, **489,** 282-U127.

Stull, R.B. Boundary-Layer Meteorol (1993) 62: 21. https://doi.org/10.1007/BF00705546

Tian, Y. D., and Coauthors, 2014: Quantifying Uncertainties in Land-Surface Microwave Emissivity Retrievals. *IEEE Transactions on Geoscience and Remote Sensing*, **52,** 829-840.

Tokioka, T., K. Yamazaki, A. Kitoh, and T. Ose, 1988: The equatorial 30-60 day oscillation and the Arakawa-Schubert penetrative cumulus parameterization. *Journal of the Meteorological Society of Japan*, **66,** 883-901.

Tulich, S. N., and B. E. Mapes, 2010: Transient Environmental Sensitivities of Explicitly Simulated Tropical Convection. *Journal of the Atmospheric Sciences*, **67,** 923-940.

Waite, M. L., and B. Khouider, 2010: The Deepening of Tropical Convection by Congestus Preconditioning. *Journal of the Atmospheric Sciences*, **67,** 2601-2615.

Wang, S., and A. H. Sobel, 2012: Impact of imposed drying on deep convection in a cloud-resolving model. *Journal of Geophysical Research-Atmospheres*, **117**.

Wulfmeyer, V., and Coauthors, 2015: A review of the remote sensing of lower tropospheric thermodynamic profiles and its indispensable role for the understanding and the simulation of water and energy cycles. *Reviews of Geophysics*, **53,** 819-895.

Xu, W., and E. J. Zipser, 2012: Properties of deep convection in tropical continental, monsoon, and oceanic rainfall regimes. *Geophysical Research Letters*, **39**.

Yeo, K., and D. M. Romps, 2013: Measurement of Convective Entrainment Using Lagrangian Particles. *Journal of the Atmospheric Sciences*, **70,** 266-277.

Zhang, G. J., and N. A. McFarlane, 1995: Sensitivity of climate simulations to the parameterization of cumulus convection in the Canadian climate center general-circulation model. *Atmosphere-Ocean*, **33,** 407-446.

Zipser, E. J., 1977: Mesoscale and convective-scale downdrafts as distinct components of squall-line structure. *Monthly Weather Review*, **105,** 1568-1589.

Figure Captions

Figure 1: a) Two example vertical thermodynamic profiles from the ERA-I dataset, presenting thermodynamic information in θ_e - based variables. The red (blue) is an example dry (moist) environment. The solid and dashed lines indicate θ_e^* and θ_e variables respectively. b) The vertical structure of the piecewise-linear mass-flux presented in (12), with different vertical gradients in three distinct lower tropospheric layers.

Figure 2: TRMM 3B42 precipitation conditionally averaged by three θ_e -based variables from ERA-I: the deep tropospheric saturation equivalent potential temperature (θ_{ed}^*), the boundary layer equivalent potential temperature (θ_{eBL}) and the lower-tropospheric subsaturation (θ_{eL}^+, axis reversed so moisture increases to the right), for four different tropical ocean regions (as defined in Section 2). The θ_e -based variables are normalized by the average saturation equivalent potential temperature in the 500 – 600 mb layer, and re-dimensionalized by a reference value (340 K). The precipitation is shown as a function of θ_{eL}^+ for different fixed values of

θ_{ed}^{*} and θ_{eBL}. In each column, θ_{eBL} increases from the top to the bottom; in each row, θ_{ed}^{*} increases from the left to the right.

Figure 3: TRMM 3B42 precipitation, conditionally averaged by four normalized θ_e-based variables from ERA-I: θ_{ed}^{*}, θ_{eBL}, θ_{eL}^{+} and θ_{eM}^{+}. (a) Precipitation as a function of θ_{eL}^{+} for different binned values of θ_{eM}^{+}, θ_{e}^{*} and θ_{eBL}, with the colors indicating different θ_{eM}^{+} values. (b) The precipitation curves for different θ_{eM}^{+} values shifted such that they all reach a specified threshold (0.95 mm/hr) at the same θ_{eL}^{+} value. (c) The average of all the shifted precipitation curves in (b); the linear extrapolation identifies the critical θ_{eL}^{+} (θ_{eLC}^{+}) at which the precipitation begins to increase sharply. (d) The scatter plot with the slope of the linear regression fit, showing how θ_{eLC}^{+} shifts as a function of different θ_{eM}^{+}.

Figure 4: As in Figure 3, but showing the relative shifts in θ_{eL}^{+} for changes in θ_{eBL}.

Figure 5: As in Figure 3, but showing the relative shifts in θ_{eBL} for changes in θ_{eL}^{+}.

Figure 6: As in Figure 3, but showing the relative shifts in θ_{eBL} for changes in θ_{eM}^{+}.

Figure 7: As in Figure 3, but showing the relative shifts in θ_{eL}^{+} for changes in θ_{ed}^{*}.

Figure 8: TRMM 3B42 precipitation conditionally averaged by ERA-I CWV and $\hat{T}$, across different tropical land regions (color) and the tropical Western Pacific Ocean (W.Pac; in black). The precipitation curves are displayed as function of increasing CWV, for fixed $\hat{T}$ bins. In each row, $\hat{T}$ increases from left to right. The different land regions are West Africa (W.Afr, @domain), India, East Asia (E.Asia), South America (S.Amer), Aus (Australia), M.Cont (Maritime Continent) and Arg (Argentina). The bounds for the different regions are defined in Section 2.

Figure 9: TRMM 3B42 precipitation conditionally averaged by B_{int}, computed from (16) using ERA-I data over (a) different tropical ocean basins: Western Pacific, Indian Ocean (Ind. Ocn), Eastern Pacific (E.Pac) and the Atlantic (Atl) and different tropical land regions referenced against the Western Pacific Ocean in (b) and (c).

Figure 10: As in Figure 8, but showing the probability density function of the precipitating (a,b and c) and the total (d,e and f) B_{int} points. A threshold of 0.25 mm/hr was used to identify the precipitating points.

Figures

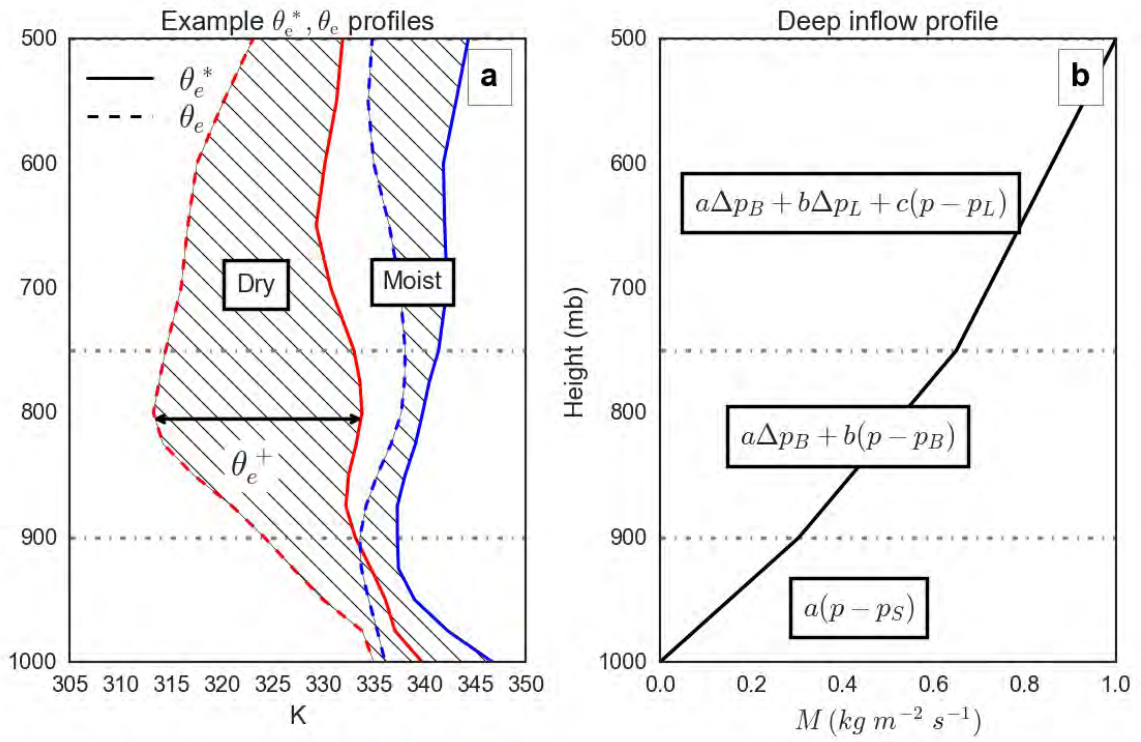

Figure 1: a) Two example vertical thermodynamic profiles from the ERA-I dataset, presenting thermodynamic information in θ_e - based variables. The red (blue) is an example dry (moist) environment. The solid and dashed lines indicate θ_e^* and θ_e variables respectively. b) The vertical structure of the piecewise-linear mass-flux presented in (12), with different vertical gradients (to be estimated empirically) in three distinct lower tropospheric layers.

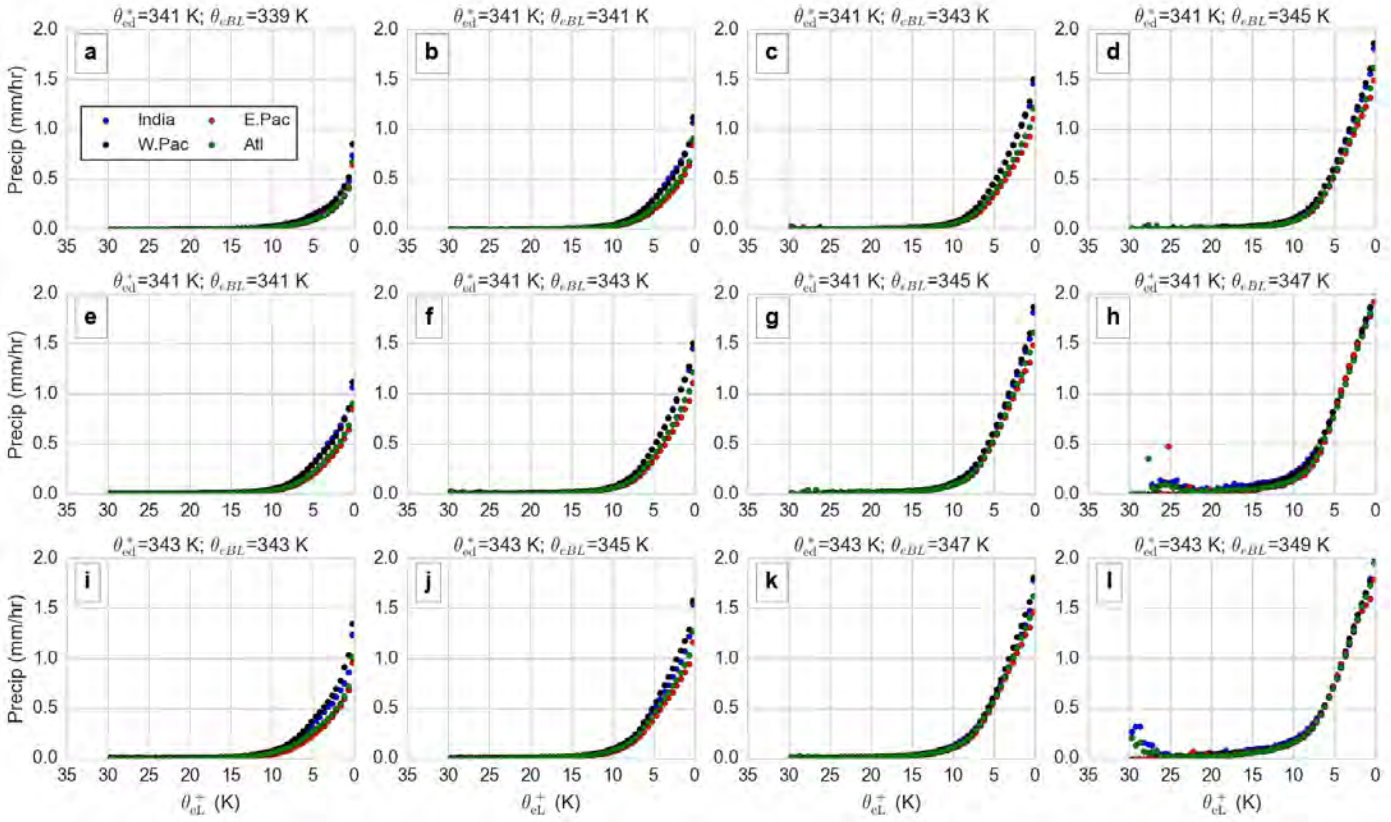

Figure 2: TRMM 3B42 precipitation conditionally averaged by three θ_e -based variables from ERA-I: the deep tropospheric saturation equivalent potential temperature (θ_{ed}^{*}), the boundary layer equivalent potential temperature (θ_{eBL}) and the lower-tropospheric subsaturation (θ_{eL}^{+}, axis reversed so moisture increases to the right), for four different tropical ocean regions (as defined in Section 2). The θ_e -based variables are normalized by the average saturation equivalent potential temperature in the 500 – 600 mb layer, and re-dimensionalized by a reference value (340 K). The precipitation is shown as a function of θ_{eL}^{+} for different fixed values of θ_{ed}^{*} and θ_{eBL}. In each column, θ_{eBL} increases from the top to the bottom; in each row, θ_{ed}^{*} increases from the left to the right.

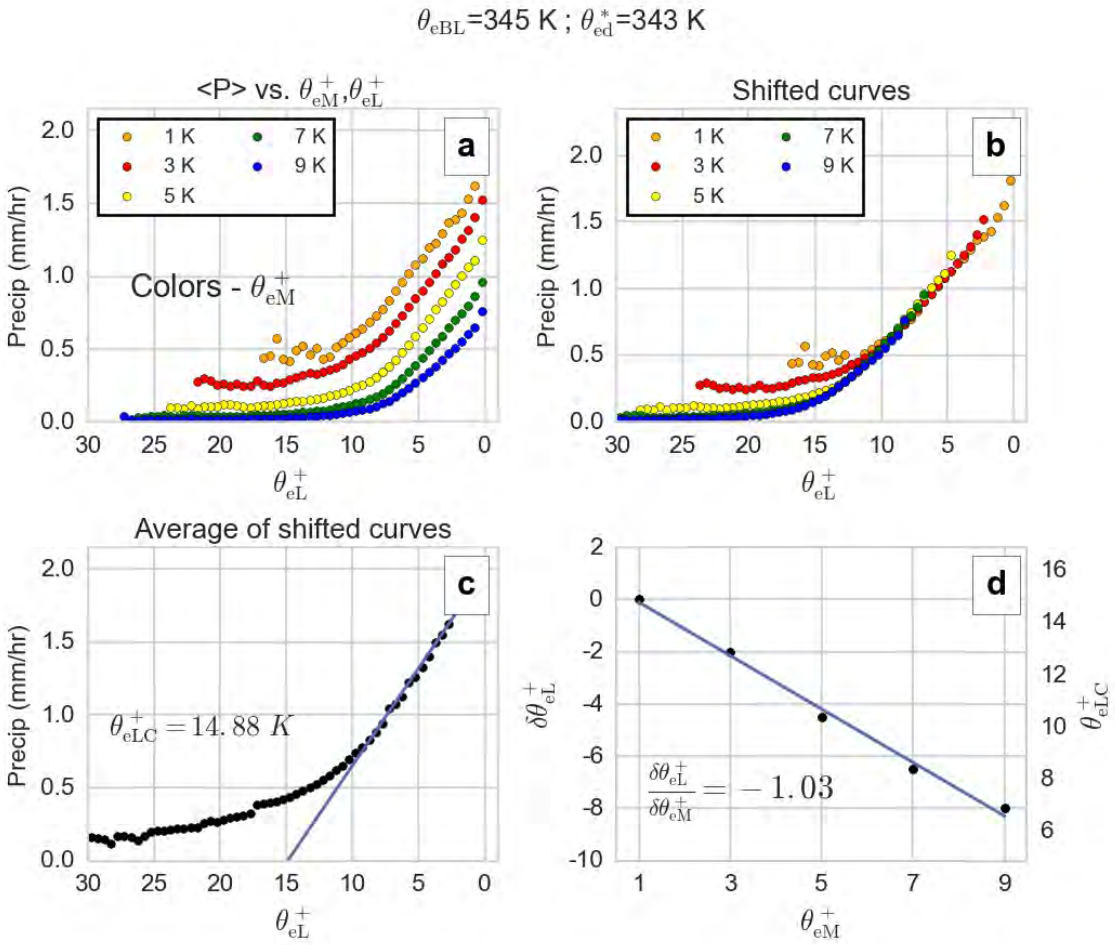

Figure 3: TRMM 3B42 precipitation, conditionally averaged by four normalized θ_e-based variables from ERA-I: θ_{ed}^*, θ_{eBL}, θ_{eL}^+ and θ_{eM}^+. (a) Precipitation as a function of θ_{eL}^+ for different binned values of θ_{eM}^+, θ_e^* and θ_{eBL}, with the colors indicating different θ_{eM}^+ values. (b) The precipitation curves for different θ_{eM}^+ values shifted such that they all reach a specified threshold (0.95 mm/hr) at the same θ_{eL}^+ value. (c) The average of all the shifted precipitation curves in (b); the linear extrapolation identifies the critical θ_{eL}^+ (θ_{eLC}^+) at which the precipitation begins to increase sharply. d) Scatter plot of the critical values with the slope of the linear regression fit, showing how θ_{eLC}^+ shifts as a function of different θ_{eM}^+.

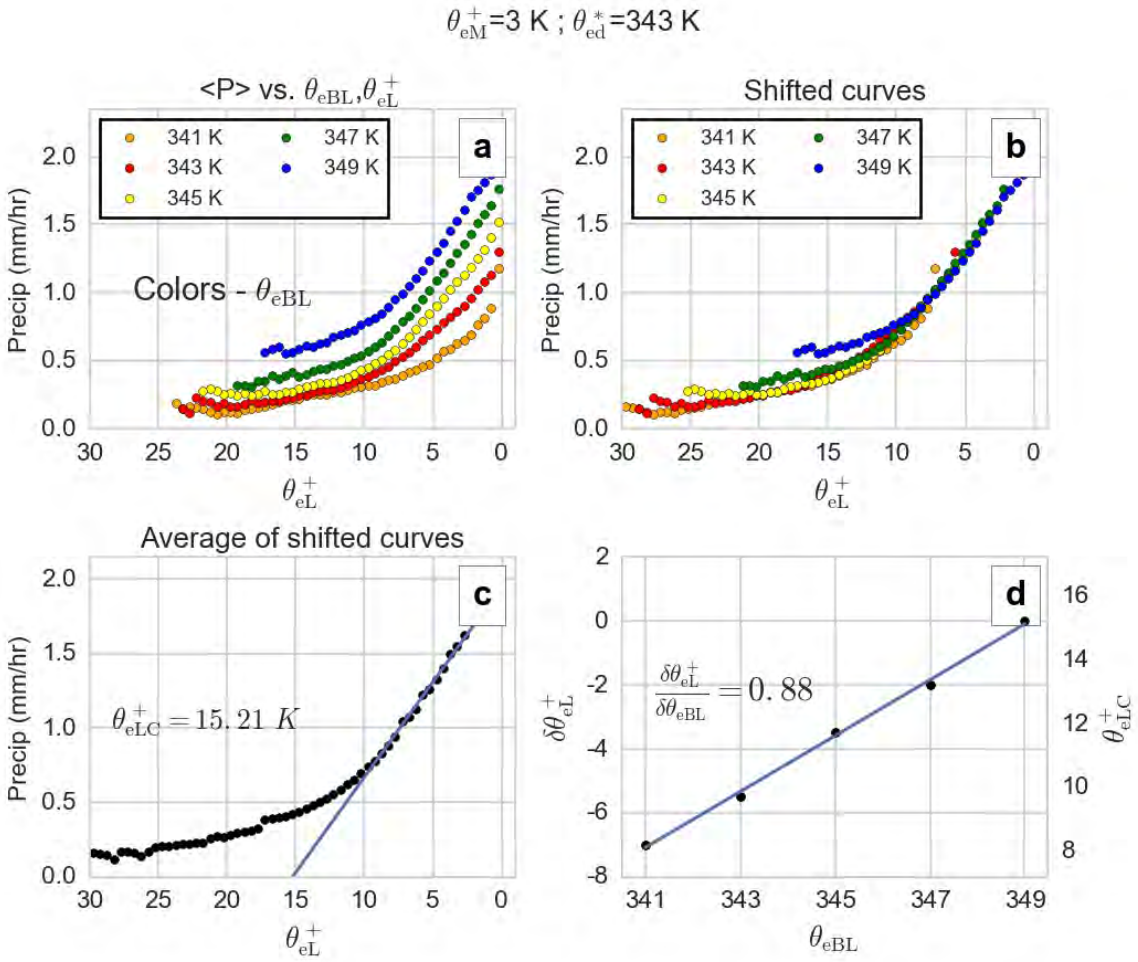

Figure 4: As in Figure 3, but showing the relative shifts in θ_{eL}^{+} for changes in θ_{eBL}.

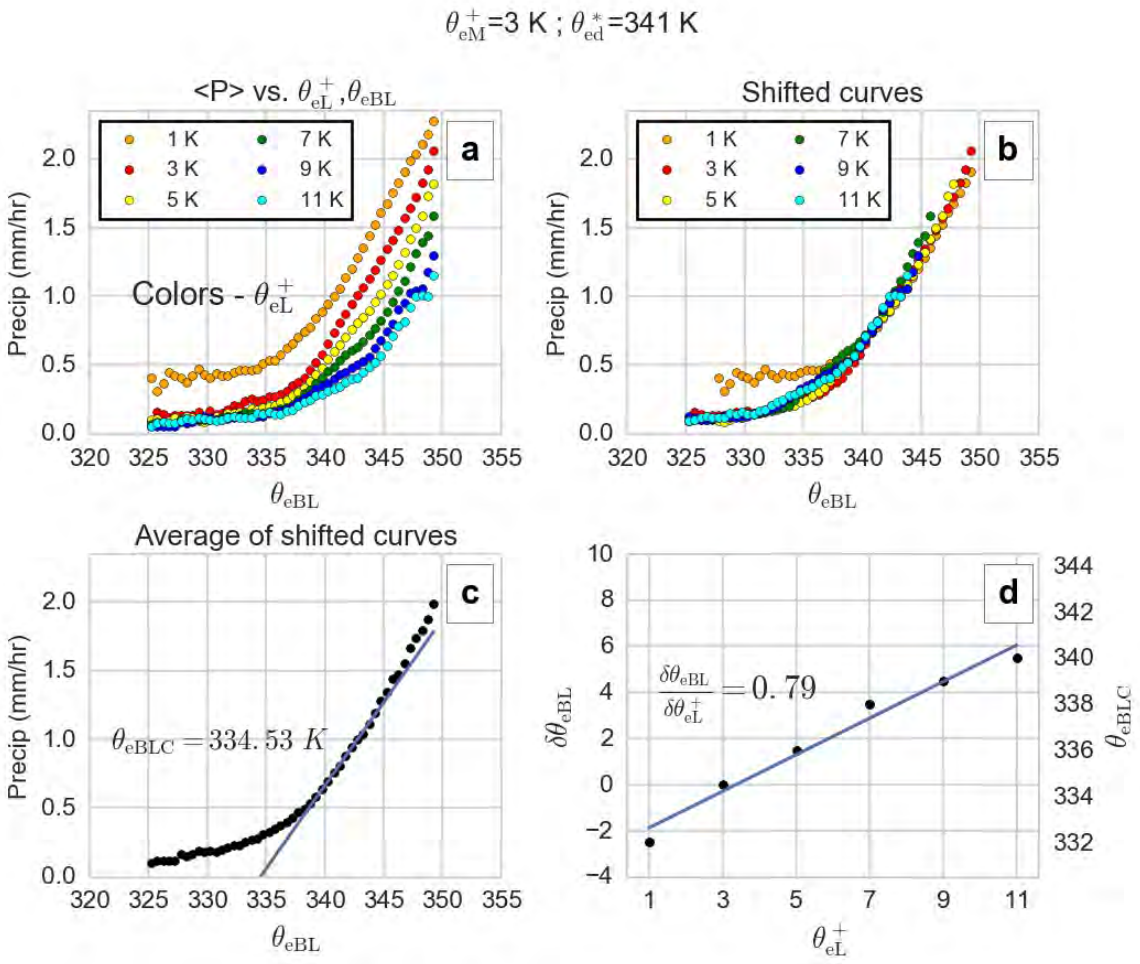

Figure 5: As in Figure 3, but showing the relative shifts in θ_{eBL} for changes in θ_{eL}^{+}.

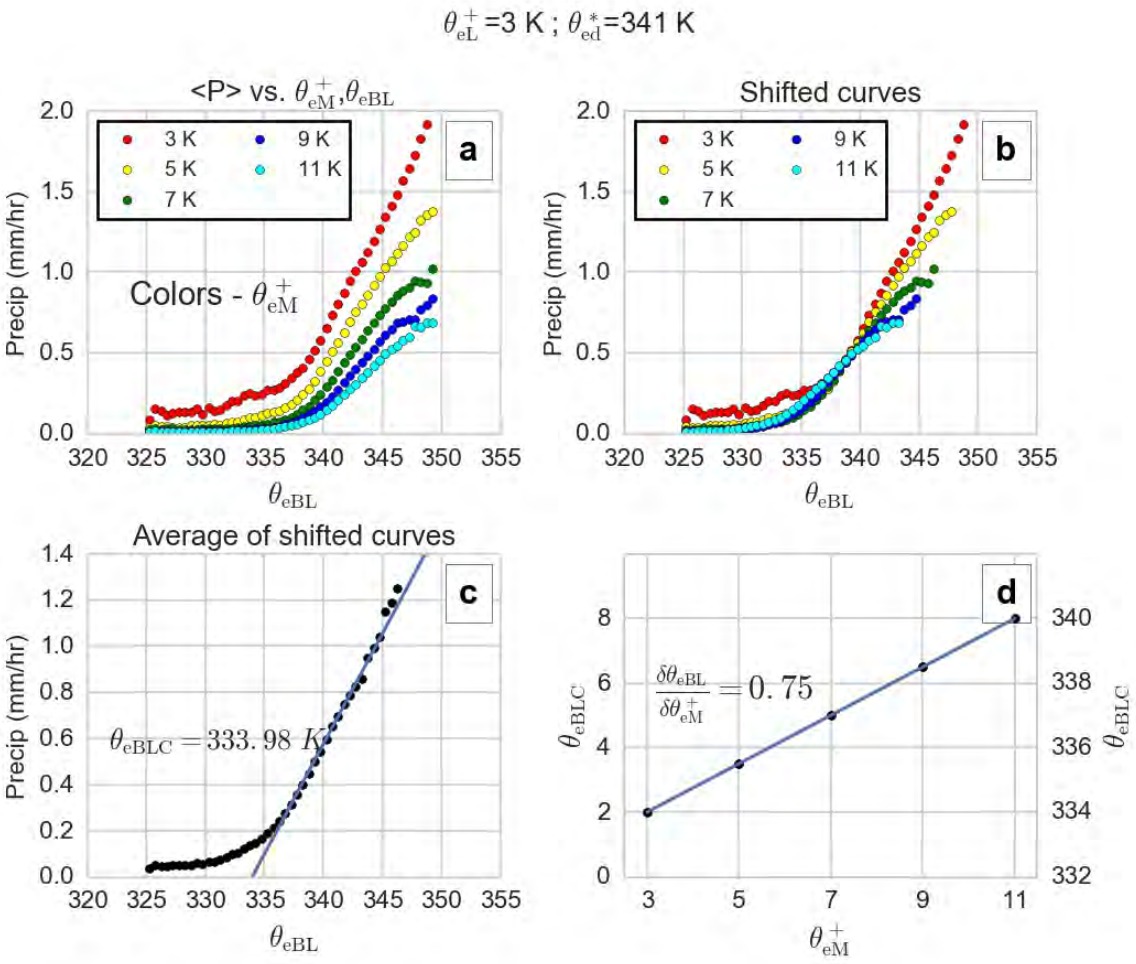

Figure 6: As in Figure 3, but showing the relative shifts in θ_{eBL} for changes in θ_{eM}^{+}.

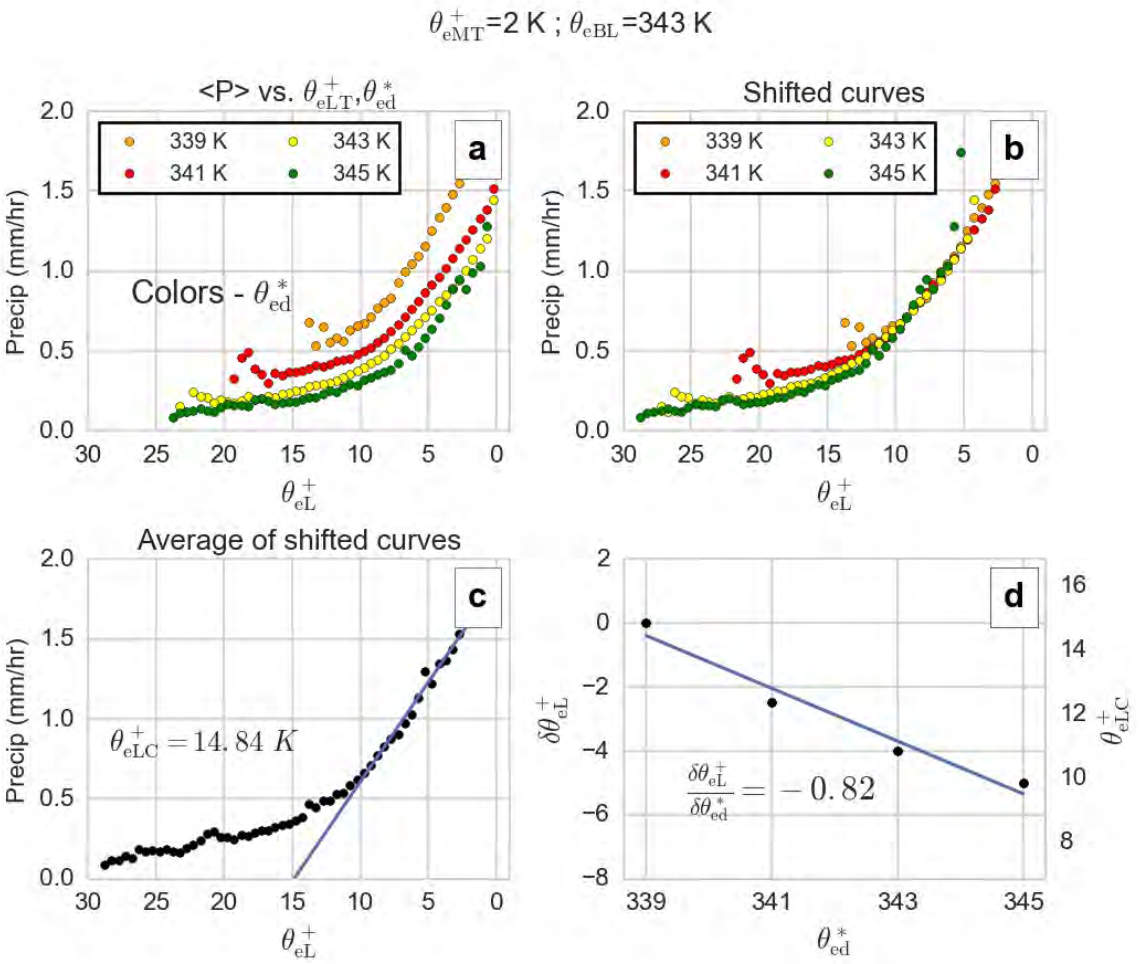

Figure 7: As in Figure 3, but showing the relative shifts in θ_{eL}^{+} for changes in θ_{ed}^{*}.

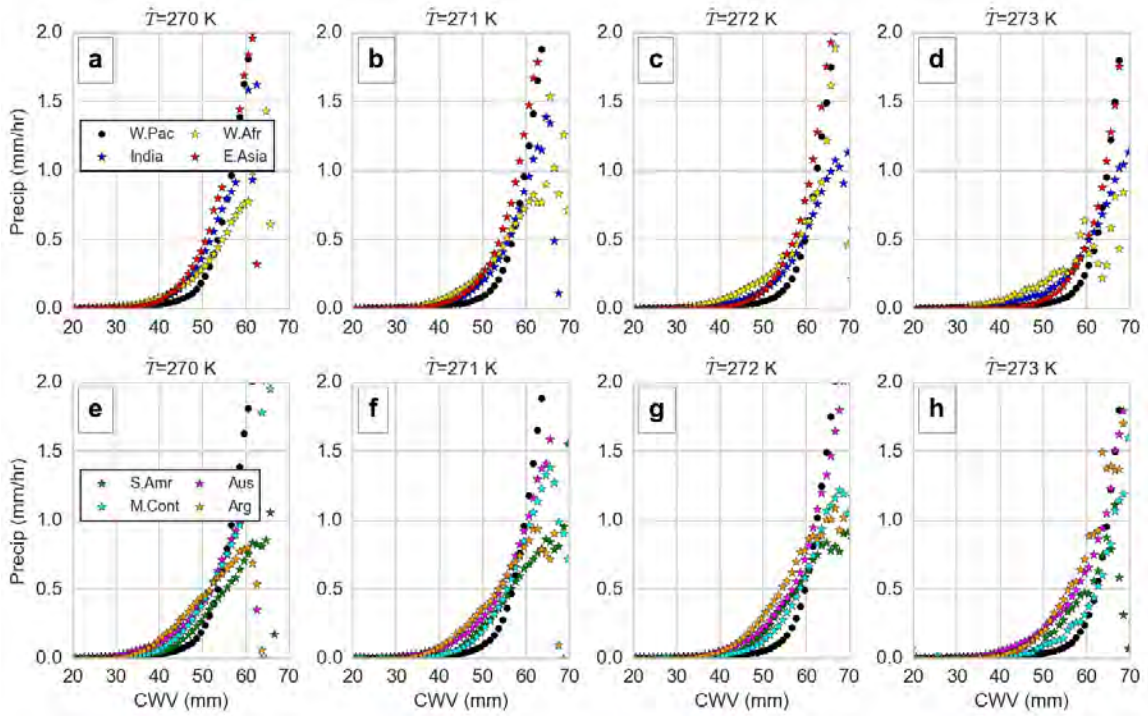

Figure 8: TRMM 3B42 precipitation conditionally averaged by ERA-I CWV and $\hat{T}$, across different tropical land regions (color) and the tropical Western Pacific Ocean (W.Pac; in black). The precipitation curves are displayed as function of increasing CWV, for fixed $\hat{T}$ bins. In each row, $\hat{T}$ increases from left to right. The different land regions are West Africa (W.Afr, @domain), India, East Asia (E.Asia), South America (S.Amer), Aus (Australia), M.Cont (Maritime Continent) and Arg (Argentina). The bounds for the different regions are defined in Section 2.

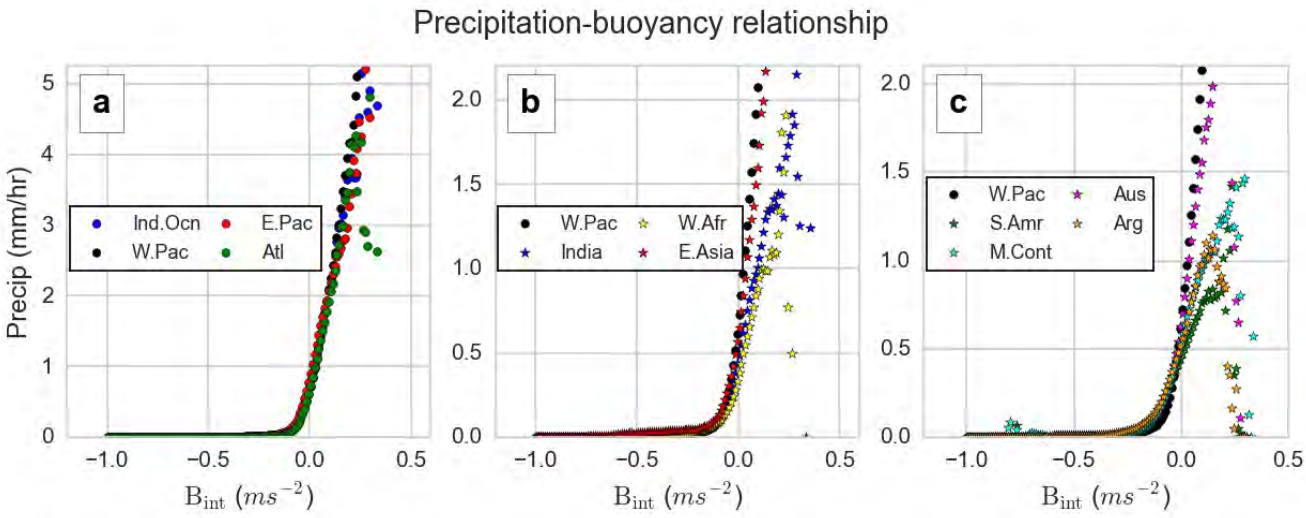

Figure 9: TRMM 3B42 precipitation conditionally averaged by B_{int}, computed from (16) using ERA-I data over (a) different tropical ocean basins: Western Pacific, Indian Ocean (Ind. Ocn), Eastern Pacific (E.Pac) and the Atlantic (Atl) and different tropical land regions referenced against the Western Pacific Ocean in (b) and (c).

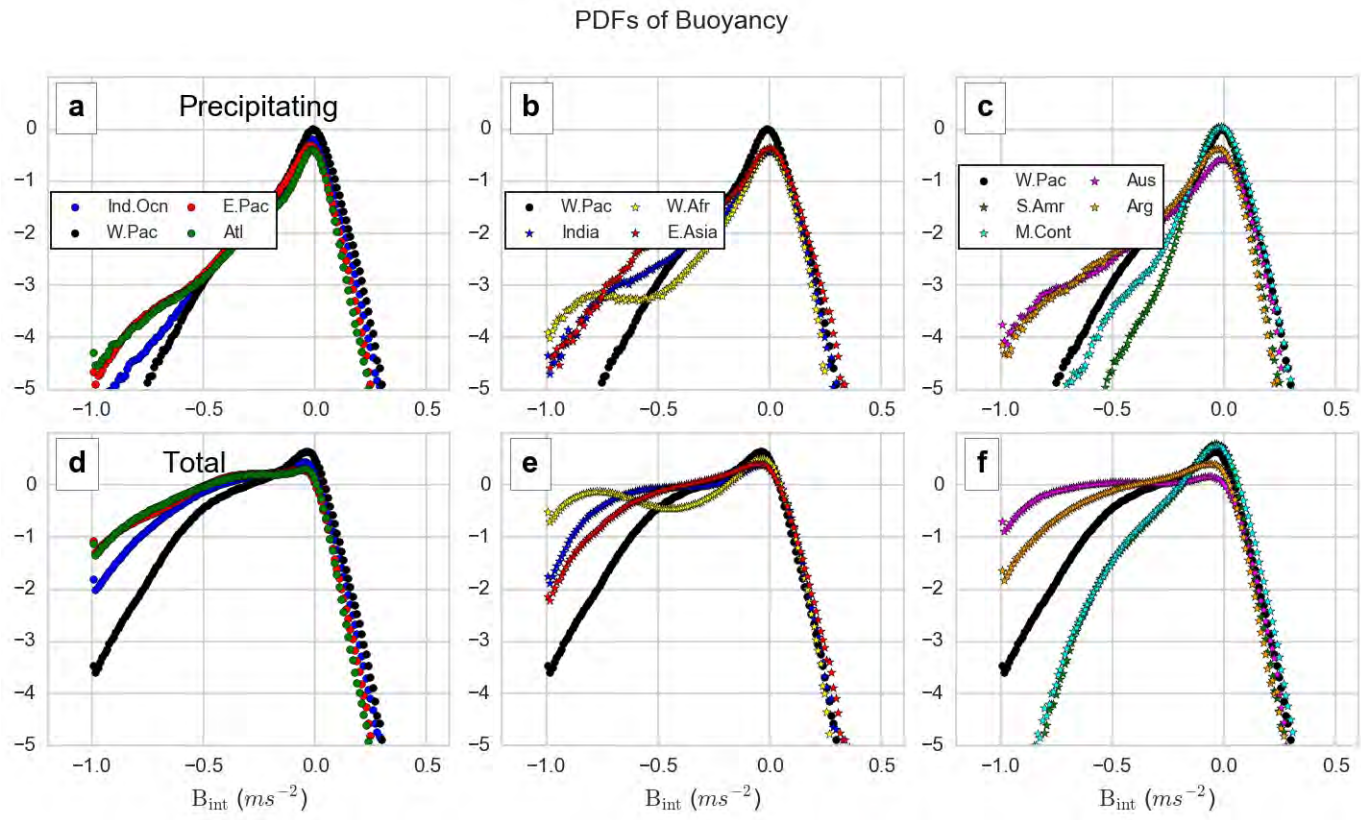

Figure 10: As in Figure 9, but showing the probability density function of the precipitating (a,b and c) and the total (d,e and f) B_{int} points. A threshold of 0.25 mm/hr was used to identify the precipitating points.